Available online at www.sciencedirect.com
SCIENCE DIRECT®

Nuclear Instruments and Methods in Physics Research A 499 (2003) 191–227

NUCLEAR INSTRUMENTS & METHODS IN PHYSICS RESEARCH
Section A

www.elsevier.com/locate/nima

Commissioning of KEKB

K. Akai[a], N. Akasaka[a], A. Enomoto[a], J. Flanagan[a], H. Fukuma[a], Y. Funakoshi[a], K. Furukawa[a], T. Furuya[a], J. Haba[a], S. Hiramatsu[a], K. Hosoyama[a], T. Ieiri[a], N. Iida[a], H. Ikeda[a], S. Kamada[a], T. Kamitani[a], S. Kato[a], M. Kikuchi[a], E. Kikutani[a,*], H. Koiso[a], S. Kurokawa[a], M. Masuzawa[a], T. Matsumoto[a], T. Mimashi[a], T. Mitsuhashi[a], T.T. Nakamura[a], Y. Ogawa[a], K. Ohmi[a], Y. Ohnishi[a], S. Ohsawa[a], N. Ohuchi[a], K. Oide[a], E. Perevedentsev[b], K. Satoh[a], M. Suetake[a], Y. Suetsugu[a], T. Suwada[a], M. Tawada[a], M. Tejima[a], M. Tobiyama[a], S. Uno[a], Y. Wu[c], N. Yamamoto[a], M. Yoshida[a], M. Yoshioka[a], S. Yoshimoto[a], F. Zimmermann[d]

[a] *KEK, High Energy Accelerator Research Organization, 1-1 Oho, Tsukuba, Ibaraki 305-0801, Japan*
[b] *The Budker Institute of Nuclear Physics Academician Lavrentyev, 11 630090 Novosibirsk, Russia*
[c] *Institute for High Energy Physics, Beijing, China*
[d] *CERN, European Organization for Nuclear Research, CH-1211 Geneve 23, Switzerland*

Abstract

KEKB has been operated since December, 1998, to deliver $B\bar{B}$ pairs for a physics detector. In this paper,we describe the commissioning procedure of KEKB.

PACS: 29.20

Keywords: Electron storage ring; High luminosity; B-meson factory; Accelerator operation; Electron-cloud instability

---

1. Introduction

At present, KEKB, which has been operated since December 1998 at KEK, is one of the most productive accelerators for particle physics. It is an energy-asymmetric double-ring collider for B-meson physics. KEKB consists of an 8-GeV electron ring (the high energy ring: HER), a 3.5-GeV positron ring (the low energy ring: LER) and their injector, which is a linac-complex providing the rings with not only an electron beam, but also a positron beam. In this paper, we describe the history of how we have operated it, or in other words, how we have been making efforts to increase the luminosity.

The organization of this paper is as follows: in Section 2, we overview problems we countered in attempts to increase the luminosity; this Section can be considered as a guide to the remainder of

---

*Corresponding author.
E-mail address: kikutani@post.kek.jp (E. Kikutani).

0168-9002/03/$ - see front matter © 2002 Elsevier Science B.V. All rights reserved.
PII: S0168-9002(02)01788-6

the paper. In Section 3, optics issues, particularly the question how we correct distorted optical functions in daily operation, are discussed. Section 4 is devoted to the description of several beam-instabilities observed in KEKB. The beam–beam issues, which can be a unique theme in two-ring colliders, are discussed in Section 5, based on our experiences. In Sections 5.3 and 5.4, we explain sophisticated beam-tuning tools developed for increasing the luminosity. In Section 6, we review the beam-background in the physics detector. Sections 7 and 8 describe special hardware developed to solve the largest problems encountered, heavy beam-background to the detector and an instability due to photo-electrons.

Though further improvements were made after the summer shutdown 2001, we restrict ourselves to describe the work until July, 2001, unless specified otherwise.

2. Luminosity boost

Fig. 1 shows the performance history of KEKB since 1999. In the 2001 run through November 11, KEKB marked the following records of the luminosity: peak luminosity, 5.17 $\mathrm{nb}^{-1}\,\mathrm{s}^{-1}$; integrated luminosity/day, 278 pb^{-1}; integrated luminosity/7 days, 1.70 fb^{-1}; integrated luminosity/month 4.79 fb^{-1}. The numbers above are all recorded values by the Belle detector. All these numbers were the highest luminosity in the history of colliders before November, 2001. Belle's integrated luminosity has also reached 38.8 fb^{-1}, which greatly contributed to the observation of CP violation in the decays of B mesons.

Table 1 gives the machine parameters corresponding to the best peak luminosity. These parameters actually deviate from the design parameters [1]. The most noticeable point is the balance of the beam currents, which are set quite differently from the so-called energy-transparent condition (inversely proportional to the beam energy). The main reason for this choice is a blowup of the LER beam due to the remaining effect of the electron cloud. The presence of the cloud in the LER limits the current below about 950 mA. Under this limitation, the HER current was raised as far as the luminosity increased, resulting in a big imbalance compared to the energy transparency.

Another deviation from the design is the bunch spacing, which is also limited by the electron-cloud effect. A bunch spacing shorter than 4 RF-buckets

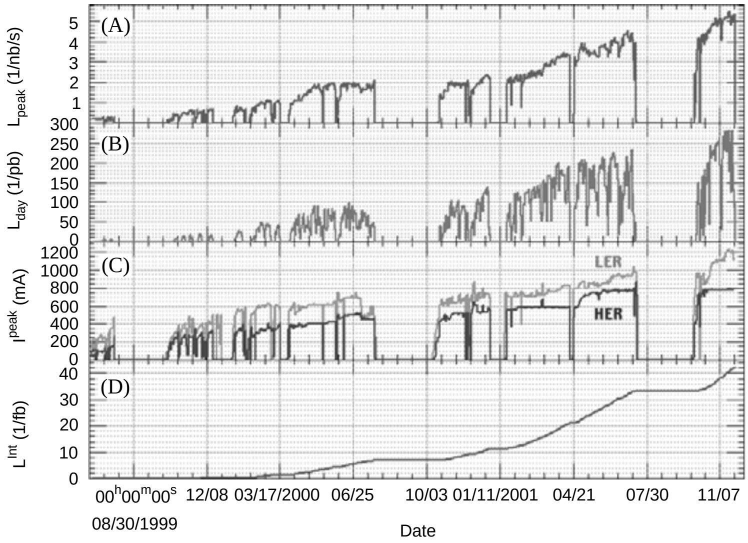

Fig. 1. History of the peak luminosity of KEKB. Also the histories of the integrated luminosity per day, peak currents of the both rings and the integrated luminosity of total runs are shown.

Table 1
Performance compared with the design up to October 31 2001

		LER		HER
Emittance (nm)	ε_x	18 (18)		24 (18)
Beta functions at IP (m)	β_x^*/β_y^*	0.59/0.0065 (0.33/0.010)		0.63/0.0070 (0.33/0.010)
Momentum compaction	α_c	3.41×10^{-4}		3.38×10^{-4}
Beam current (mA)	I_{beam}	1072 (2600)		761 (1100)
Number of bunches	N_b		1153 ($\sim$5000)	
Bunch current (mA)	I_{bunch}	0.93 (0.52)		0.66 (0.22)
Bunch spacing (ns)	τ_{sp}		8 (2)	
Bunch length (mm@MV)	σ_l	6–8@6.0 (3.4@6.5)		Not measured (5.5@12.0)
Beam–beam parameters	ξ_x/ξ_y	0.073/0.047 (0.039/0.052)		0.061/0.035 (0.039/0.052)
Betatron tunes	ν_x/ν_y	45.51/43.57 (45.52/44.08)		44.52/41.59 (44.52/42.08)
Synchrotron tune	ν_s	−0.0223		−0.0199
RF voltage (MV)	V_c	6.5		12.0
Lifetime (min@mA)	τ_{beam}	101@ 1072		266@761
Luminosity ($\text{cm}^{-2}\ \text{s}^{-1}$)	L		5.17×10^{33} (1.0×10^{34})	

Values in parentheses are the design values.

(8 ns) did not give a better luminosity, probably due to a mixed effect of the beam–beam and the electron cloud.

The vertical beta functions at the interaction point (IP) were squeezed to a value smaller than the design to extract more luminosity from the given beam current. Other parameters, such as the horizontal beta functions and the emittances, were chosen empirically by optimizing the luminosity.

We now describe the significant improvements made to increase the luminosity applied until July, 2001.

2.1. Higher beam currents

As shown in Fig. 1, the beam currents of both the LER and HER were increased during this period. The most significant factor to enable the higher currents in the LER was additional solenoid coils for suppressing the electron-cloud effect. During the summer shut down of the year 2000, solenoids were wound in the arc of the LER for about 800 m, with a strength of around 50 G. Its effect was confirmed by both the single-beam beam size and the luminosity by the end of 2000. The suppression of the electron-cloud effect by the solenoids was limited to below 650 mA. In January of this year, more solenoids for about 500 m were added. The new solenoids contributed to the decrease in the vertical beam size during collisions for beam currents higher than 650 mA, and made a high-current operation of the LER up to 930 mA possible. Their beneficial effect was also confirmed until June for both single and colliding beams.

As for the HER, the current limit had been determined by the heating of the movable masks in the arc due to their resonant modes. In April 2001, these masks were replaced by new moving-chamber types, which had been successfully applied in the LER last year. Since the new ones do not have significant resonances, they are no longer the limiting factor of the beam current in the HER. As a result, the HER current was increased from 560 to 800 mA by July.

The storage of single-beam currents was tested up to 1050 mA in the LER and 870 mA in the HER, respectively. The latter number was the highest record ever achieved by superconducting RF cavities. Although the limitation of the beam current is given by other conditions, a bunch spacing shorter than 4 buckets will be necessary to avoid heating of some vacuum components by the short bunch wakes. Hence, for a higher luminosity, increasing the number of bunches is necessary.

2.2. Better collision parameters

The second reason for the high luminosity during this year was a better choice of the beam parameters, such as the betatron tunes and the beta functions at the interaction point. First, the vertical tunes were raised from about 0.08 to around 0.57 in the both rings. This change improved the stability of the vertical orbit at the interaction point and in the entire ring. It also contributed to stabilize the vertical dispersion and the x–y coupling. While the peak luminosity was not worse than for the old tune, the average luminosity was clearly improved.

Before last year the horizontal tunes were set at around 0.52, very close to the half-integer resonance. In March 2001, the horizontal tune was made even closer to the resonance, 0.51, or below. The luminosity was improved by about 20% by this change. An explanation is the so-called dynamic beta effect, which is maximized at the half-integer resonance. This ultimately close-to-the-resonance tuning was made possible by a precise beam-optics correction and the establishment of the monitoring and control of the betatron tunes.

The vertical beta functions were squeezed down to 6.5 mm (LER) and 7 mm (HER), which are well below the design value (1 cm). The horizontal beta functions were still bigger than the design value, but were the result of tuning to optimize the luminosity with the limitation on the detector background.

2.3. More stabilization

The third reason for the higher luminosity were various improvements in the hardware and software to keep the machine more stable at higher beam currents and smaller beam sizes. The betatron tunes were always monitored by collision-free pilot bunches. They were kept at the best empirical curves as a function of the beam current. The beam optics, such as beta beats, dispersions, and x–y couplings, were regularly measured and corrected, typically once in 2 weeks after a standardization of the magnets. The optics correction was made by an online modeling system with SAD, taking 20–30 min per ring.

The drifts of the circumference of the two rings were observed to be about 300 μm out of 3 km during 1 day, and 2 mm during 1 year. Some correlation with the air temperature was seen. The change in the circumference causes the drift of the horizontal orbit, which causes serious optical errors with strong sextupoles. A new feedback system to correct the circumference by changing the RF frequency (HER) or chicane (LER) was successfully applied during this period to solve this problem.

Tuning and feedback methods of the colliding orbits and the beam sizes were highly developed during this period. Sophistications of these feedback tools were achieved in suppressing the flip–flop effect in the horizontal beam sizes with the strong beam–beam parameters (about 0.07) and the dynamic beta, dynamic emittance effects. Much progress was made in data-logging and archiving. A number of tools were developed to make history plots and correlations.

The heating of various hardware components has been a big issue for high-current operation. More water channels and cooling fans were attached on the chambers around the interaction point, movable masks, bellows chambers, ceramic chambers for the injection/abort kickers, etc. A special adjustment of the length of the bellows was made for the bellows near the movable masks to avoid any parasitic resonance due to deformed TE modes. A careful study of the higher-order modes of the chamber at the interaction point showed a good agreement with a prediction by the model for a 5-bucket spacing. This was a very useful study for a future upgrade of the IP chamber.

Though the new movable masks eliminated heating due to the higher-order modes, damage to the mask, itself, occurred because of a big beam loss at the masks. A few scratched lines with 1 mm width and a few mm depth were seen at the masks after operation for a few months. To prevent further damage, fast beam-loss monitors using PIN diodes were utilized to abort the beam as quickly as possible. Another fast beam-abort system was developed to detect any phase deviation of the beam at the RF cavities, in case one of them is tripped. These systems surely contributed to reduce the damage at the masks. A further improvement of the masks, however, is necessary to solve this problem completely. The introduction of a spoiler-type mask made of light metal can be a good candidate.

2.4. Issues of the electron cloud

To raise the luminosity we must increase the number of bunches by reducing the bunch spacing. Up to now, the bunch spacing has been chosen to be 4 buckets (8 ns) in most physics runs. With the 4-bucket spacing, the beam current has nearly reached the limit given by the bunch current. Since a shorter bunch spacing is necessary for a higher luminosity, 3-bucket and 2-bucket spacings were tried several times. The result was very curious. Let us consider the specific luminosity per bunch (luminosity/bunch/(product of bunch charges)). It is basically the inverse of the beam area at the IP. When the beam–beam effect is the dominant source of beam blowup, the specific luminosity per bunch should increase for smaller bunch currents. When we keep the total current constant and reduce the bunch spacing (or increase the number of bunches), the specific luminosity per bunch should increase. The observation in KEKB was that the specific luminosity per bunch did not improve at all for bunch spacings shorter than 4 buckets, and actually remained almost unchanged. The specific luminosity per bunch was nearly the same for 4-, 3-, 2-bucket spacings for a given total current of the LER, that is, the beam size in collision behaves as if it is determined by the LER total current due to the electron cloud. On the other hand, the beam size measured by the interferometer was significantly larger in collision than in the single-beam case, for a given current. A peculiar feature is that the specific luminosity decreases below the threshold intensity of the single-beam blowup. It gradually decays as the beam current increases, showing no threshold behavior.

An interpretation of these observations for a shorter bunch spacing is still under discussion. It can be neither a simple beam–beam effect nor a single-beam effect. It can be a mixed effect of the beam–beam and the electron cloud, but this has not yet been identified. In any case, with the new solenoids, the effect of the electron cloud was weakened, but not eliminated. The single-beam size shows a blowup at a beam currents higher than 800 mA. A new set of solenoids will be installed in the arcs during the summer shutdown of 2001 in order to further reduce the cloud.

3. Optics issues

The KEKB storage rings [1], the LER and the HER, have been designed as a high-luminosity collider with low-β optics. To achieve large dynamic apertures, the noninterleaved chromaticity-correction scheme [1,2] has been adopted. Fifty-two pairs of sextupole magnets connected with a pseudo $-I$ transformer are installed in the arcs of each ring. In addition, only in the LER, two vertical pairs are placed in the interaction region (IR) for a local chromaticity correction [1,2]. Both rings are now being operated with lower-β optics than the design: $\beta_x^*/\beta_y^* = 59/0.65$ cm for the LER and 63/0.70 cm for the HER.

It is essential for stable operation at a high luminosity to measure the optical functions, such as β-functions, dispersions and the horizontal–vertical couplings (x–y couplings), and to correct them in suitable ways. It is also important that such corrections can be done in on-line mode during daily beam operation. In KEKB, both design work and operation software have been unified within a framework of Strategic Accelerator Design (SAD) [3] developed at KEK. Thus, an on-line correction system is easily constructed using the same model-lattice as in the design and off-line analysis.

3.1. Global correction

In the KEKB rings, each quadrupole magnet is equipped with a beam position monitor (BPM). Those BPMs give only a beam-position averaged over a few seconds. Therefore, special methods represented here have been devised to obtain the optical functions without any turn-by-turn beam-position information. Three kinds of global corrections over the ring, that is, corrections for (1) β-functions, (2) dispersions and (3) x–y couplings, are applied during usual beam operation. In those corrections, two kinds of knobs are utilized:

- correction factors (*fudge factors*) for power supplies of quadrupole magnets, and
- symmetric/anti-symmetric orbit bumps at sextupole pairs.

Those corrections are made at low beam-currents ($\sim$20 mA) each time after standardization of the magnets, or when a significant degradation of the luminosity occurs. All of the calculations concerning optics correction have been made with SAD; the operation panels are also coded with the SADScript language [3].

3.1.1. Correction of the β functions

The β functions can be measured by analyzing single-kick orbits produced by kicks at several source points (k). As is well known, a displacement at the ith BPM kicked by a steering magnet at k is given as

$$\begin{aligned} x_{ik} &= f_k\sqrt{\beta_i}\cos(\pi\nu - |\mu_i - \mu_k|) \\ &\equiv F(i, \beta_i, \mu_i, f_k, \mu_k) \end{aligned} \tag{1}$$

where $\mu_{i,k}$ are the betatron phases at BPMs and kicks and f_k is expressed by

$$f_k = \frac{\sqrt{\beta_k}}{2\sin\pi\nu}\theta_k.$$

Here, θ is the kick angle and ν is the betatron tune. Eq. (1) can be rewritten in two ways as,

$$\begin{aligned} x_{ik} &= \sqrt{\beta_i}\cos(\pi\nu \pm \mu_i) f_k \cos\mu_k \pm \sqrt{\beta_i}\sin(\pi\nu \pm \mu_i) \\ &\quad \times f_k \sin\mu_k \equiv F_{\text{kick}} \end{aligned} \tag{2}$$

$$\begin{aligned} &= f_k\cos(\pi\nu \pm \mu_k)\sqrt{\beta_i}\cos\mu_i \\ &\quad \mp f_k\sin(\pi\nu \pm \mu_k)\sqrt{\beta_i}\sin\mu_i \equiv F_\beta. \end{aligned} \tag{3}$$

In order to obtain β_i, Eqs. (2) and (3) are used alternately as follows:

1. $\sqrt{\beta_i}$ and μ_i, that is, $\sqrt{\beta_i}\cos(\pi\nu \pm \mu_i)$ and $\sqrt{\beta_i}\sin(\pi\nu \pm \mu_i)$, are evaluated by the model lattice in which ν is the same as the measured value.
2. $f_k\cos\mu_k$ and $f_k\sin\mu_k$ are obtained by a linear fitting which minimizes a parameter:

   $$\sum_{i,k}(x_{ik,\text{meas}} - F_{\text{kick}})^2$$

   keeping $\sqrt{\beta_i}\cos(\pi\nu \pm \mu_i)$ and $\sqrt{\beta_i}\sin(\pi\nu \pm \mu_i)$ equal to the values determined in the previous step, using Eq. (2).
3. $\sqrt{\beta_i}\cos\mu_i$ and $\sqrt{\beta_i}\cos\mu_i$ are obtained by a linear fitting which minimizes another parameter,

   $$\sum_{i,k}(x_{ik,\text{meas}} - F_\beta)^2$$

   keeping $f_k\cos(\pi\nu \pm \mu_k)$ and $f_k\sin(\pi\nu \pm \mu_k)$ constant to be the values determined in the previous step, using Eq. (3).

The steps 2 and 3 are repeated until the condition for convergence is satisfied.

In usual corrections, the β-functions are estimated using orbits produced by six different kicks. If dispersion exists at the kick point, it is necessary to subtract its contribution. In most cases, the fitting converges within 500 iterations. In the horizontal plane, more iteration times are needed than in the vertical, because the horizontal tune is closer to the half-integer ($\sim$0.515).

The observed deviations of β-functions are corrected by applying fudge factors to the power supplies of the quadrupole magnets. The magnitudes of fudge factors are calculated with analytic response based on the model lattice. In the KEKB rings, many of the quadrupole magnets are grouped into 7 families and are connected to a small number of power supplies. Moreover, 6 out of 7 families in the arcs are not changed to keep the pseudo-I transformation between the non-interleaved sextupoles. Thus, gradient error of each quadrupole cannot be corrected. Even with those constraints, the β functions are corrected to be typically $(\Delta\sqrt{\beta})/\sqrt{\beta_{\rm model}} \leqslant 0.05$ and the betatron phases to $\Delta\phi \leqslant 2^\circ$, as shown in Fig. 2.

3.1.2. *Horizontal–vertical coupling correction*

The x–y couplings are estimated by observing the vertical leakage orbits associated with the horizontal single-kick orbits. Both skew quadrupoles in the IR (8 magnets in the LER and 12 in the HER) and symmetric vertical bumps at the SD sextupole pairs are used as correctors. Because of the pseudo -I transformation between the non-interleaved sextupoles, the symmetric bumps mainly produce an x–y coupling with cancellation of the vertical dispersion. On the other hand, asymmetric bumps are used in the dispersion correction discussed in Section 3.1.3. The strengths of the skew quadrupoles and the heights of the bumps are calculated with analytic responses based on the model lattice.

Since there are four independent coupling elements in the four-dimensional betatron phase space, more than four independent coupling observations are needed for a full correction. Usually, vertical leakage orbits are measured by horizontal kicks of 50 μrad at six different points. Those kicks produce horizontal orbits whose peaks are 1 mm in the arcs. The vertical orbits are reduced to $\Delta y_{\rm rms} \leqslant$ 20 μm in a typical correction as shown in Fig. 3. In particular, in the HER, the skew quadrupoles have been inevitable for the correction. Without them, the coupling in the IR was not able to be effectively corrected. This method corrects the x–y coupling globally, thus reducing the vertical emittance.

3.1.3. *Dispersion correction*

The horizontal and vertical dispersions are measured by changing the RF frequency, and are corrected by creating asymmetric bumps at the SF and SD pairs in the horizontal and vertical planes, respectively. Because of the pseudo-I transformation between the sextupole pairs, a pair of asymmetric bumps works as a dispersion corrector without affecting the β function and the x–y coupling. The bump heights are calculated with responses obtained by simulations with the model lattice.

In most cases, the rms deviations of the dispersion in both the horizontal and vertical planes, $\Delta\eta_{x,\rm rms}$ and $\Delta\eta_{y,\rm rms}$ were corrected to be less

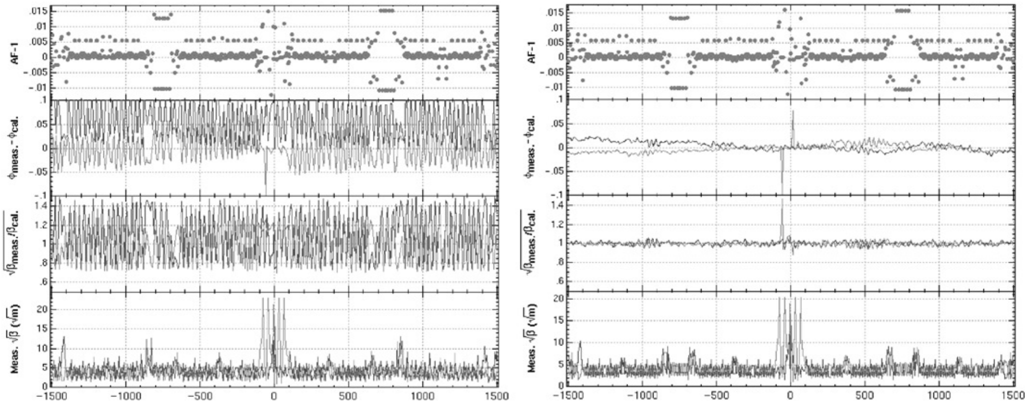

Fig. 2. Example of the β correction in the LER before (left) and after (right) a correction. Each shows the fudge factors, the betatron phase difference $\Delta\phi$, the ratio of $\sqrt{\beta_{\rm meas}}/\sqrt{\beta_{\rm design}}$ and the measured $\sqrt{\beta_{\rm meas}}$, from top to bottom. The blue (red) lines show the horizontal (vertical) data. The IP is located at $s=0$. The left figure shows the β-functions observed after a long shut down, so the deviations are much larger than those during usual operation. In this example, $(\Delta\sqrt{\beta})\sqrt{\beta_{\rm design}}$ was decreased from 0.291(0.321) to 0.042(0.043) in the horizontal (vertical) plane.

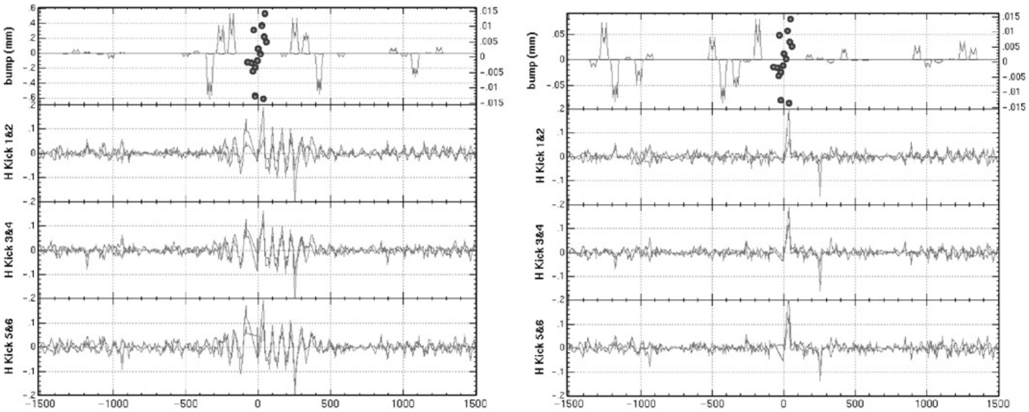

Fig. 3. Example of an x–y coupling correction in the HER, before (left) and after (right) the correction. Each shows the bumps and field gradients of skew quadrupoles required for the correction, the vertical leakage orbits (two in each graph), from top to bottom. The average rms value of the vertical orbits $\Delta y_{\rm rms}$ decreased from 26.7 to 19.4 μm in this example. Only with the bumps at the sextupoles, the correction was improved very little.

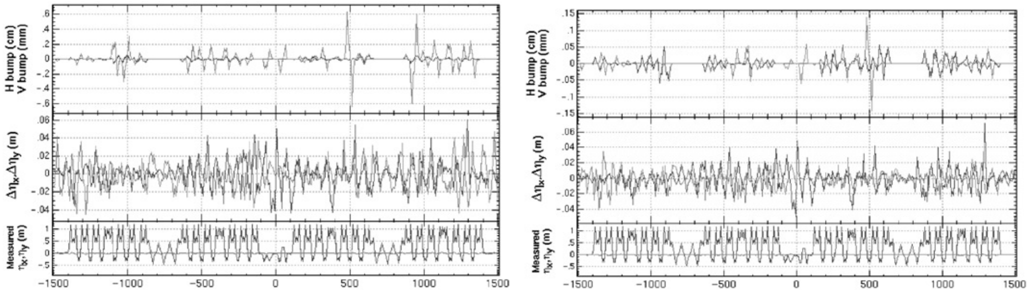

Fig. 4. Example of an η correction in the LER, before (left) and after (right) the correction. Each shows the bumps required for the correction, the differences of the dispersion $\Delta\eta_{x,y} = \eta_{\rm meas} - \eta_{\rm design}$ and the measured, $\eta_{\rm meas}$, from top to bottom. The blue (red) lines show the horizontal (vertical) data.

than 2 cm as shown in Fig. 4. The vertical dispersion at the IP was also reduced to be less than 1 mm, which was estimated with the closest BPMs, named OctoPos.

The global optical functions have been successfully corrected with three kinds of corrections in both rings. Local bumps at the sextupoles are fully utilized, as summarized in Table 2. Although these corrections, in principle, affect each other, the interference among them is not very large. Thus, corrections converge well in sequential repetitions of a few times. After the correction, the vertical-to-horizontal emittance ratio was reduced to less than 1% in both rings, where the vertical beam size was measured by a synchrotron light interferometer [4].

Table 2
Usage of sextupole bumps

Sextupole	Plane	Symmetric	Asymmetric
SF	x	$\Delta\beta$[a]	$\Delta\eta_x$
SD	y	x–y coupling	$\Delta\eta_y$

[a] The horizontal symmetric bumps at the SF sextupoles are not used in the usual β correction.

3.2. Local correction at the IP

After a global correction, the optical functions at the IP are adjusted locally in various ways to optimize the luminosity during physics runs. In this correction, the following optical parameters are measured and corrected:

- *Waist*. The waist of the vertical β-function in each ring is adjusted independently by changing the fudge factors of the final-focus quadrupoles on both sides of the IP, QCSs and QC1s (the second final-focusing quadrupoles only in the HER), with imposing the matching condition that the vertical tune constant. The β-functions in the rest of the rings are not affected by this correction, because the β beatings due to the change of the final quadrupoles are cancelled on both sides of the IP.
- *Coupling*. The four coupling parameters at the IP are adjusted by changing the skew quadrupoles, keeping the condition that the coupling should be localized within the skew area.
- *Dispersion*. The vertical dispersion and its derivative at the IP are adjusted independently by four asymmetric bumps at the four closest SD pairs (two on each side of the IP). The dispersion produced by this knob is localized within the bump area.

3.3. Continuous closed-orbit correction

The *golden* orbits determined by global and local corrections are maintained with continuous closed-orbit corrections every 20–30 s (CCC). All of the horizontal (vertical) steering magnets placed close to horizontal (vertical)-focusing quadrupoles are used in corrections with an SVD (a Singular Value Decomposition) solver in the horizontal (vertical) plane. To avoid a gradual shift of the beam energy, a sum of the kick angles of the horizontal correctors $\Sigma\,\theta_x$ is kept constant.

In order to avoid horizontal symmetric displacements at the sextupole pairs, which affect the β-functions, it is also important to maintain the orbit length in the dispersive regions (in the arc and in the area for a local chromaticity correction in the LER). In particular, in the LER, a symmetric displacement at the local correction sextupoles has a large effect on β_y^*, because of the large β_y at those sextupoles. (A displacement of 10 μm produces a $\Delta\beta_y/\beta_y^*$ of 0.03.) In the LER, the orbit length can be adjusted in the special region called *chicane*, which consists of four dipole magnets. In this region changes in the orbit and the dispersion are localized, even if the bending angle is changed. This orbit-length correction is very effective to keep the horizontal orbit unchanged. In the HER, there is no special region for the orbit-length correction, so the orbit-length drift in the arc is compensated by controlling $\Sigma\,\eta_x\theta_x$ of the horizontal correctors. If a large deviation of the orbit length is observed in the HER, the RF frequency is changed to compensate it.

4. Beam instabilities

4.1. Vertical beam blowup in the LER

A blowup of the vertical beam size has been observed in the LER, since the early operation periods [5–7]. The beam size started to increase at a threshold beam-current, and was almost doubled at 300 mA under typical operating conditions. This blowup is one of the most serious problems limiting the luminosity of KEKB. The main characteristics of the blowup observed by the interferometer are summarized as: (1) the blowup is a single beam and a multibunch effect, (2) the blowup has a threshold intensity which is determined roughly by (bunch current)/(bunch spacing), (3) no dipole oscillation has been observed when the vertical chromaticity is high (5–8), (4) the blowup is almost independent of the betatron tunes and (5) no blowup is observed in the horizontal plane. Further studies showed that (6) the tune of the bunch measured by a gated tune meter increased along the train, as shown in Fig. 5, (7) the vertical beam size measured with a fast gated camera also increased along the train and (8) the blowup became weaker when the vertical chromaticity was increased.

A model to explain the blowup has been proposed by F. Zimmermann and K. Ohmi. In their model the blowup is explained as a single-bunch head–tail instability due to a large number of electrons produced by photoemissions or secondary emissions [8,9]. The electron cloud is accumulated along a bunch train. The tune shift is roughly consistent with a calculation based on the

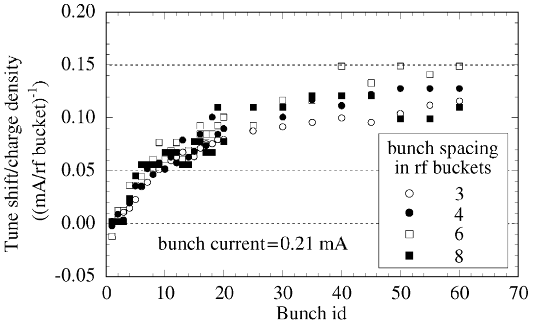

Fig. 5. Vertical betatron tune shift along the train for four different bunch spacings of 3, 4, 6 and 8 RF buckets. The tune shift is normalized by the charge density of the beam (I_b/S_b).

model, and the threshold bunch-intensity of the blowup is consistent with the threshold of the transverse mode-coupling instability.

To cure the blowup, many C-shaped permanent magnets, named C-yokes, were attached to vacuum chambers in the arcs to confine the electrons to the vicinity of the chamber wall. In September 2000, the C-yokes were replaced by solenoid magnets to confine the electrons more efficiently, as indicated by a simulation. The total length of the solenoids was about 800 m and the calculated field strength was 45 G at the central axis of the solenoid. In Section 8, we describe the structure of these solenoids as well as a procedure of their installation.

After these solenoids were wound, the blowup was reduced, even though the suppression was not complete. Indeed, as shown in Fig. 6, the threshold current of the blowup increased when the solenoid was excited. A measurement by a fast gated camera shows that the solenoids were effective to suppress the blowup, especially in the forward part of the train, as shown in Fig. 7. The effect of the solenoids was also confirmed by the measurement of the luminosity (see Fig. 8). In Fig. 8, the luminosity per bunch increases by a factor 1.6, when the solenoids are excited.

4.2. Transverse coupled-bunch instability

During the routine operation in KEKB, beam currents of 900 and 800 mA are stored in the LER and HER, respectively. The transverse coupled-bunch instability (TCBI) is well suppressed by the transverse bunch-by-bunch feedback systems in both rings, so that the TCBI is not a limiting factor to store the beam at present level of the beam currents. However, the TCBI may still become a limitation in high-current operations with shorter

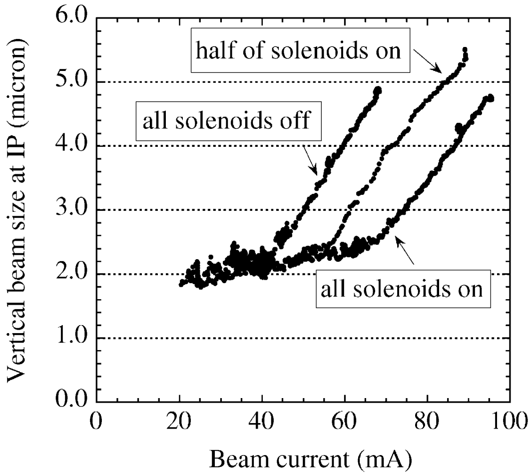

Fig. 6. Vertical beam size as a function of the beam current. In the measurement, two trains were injected on opposite sides of the ring. Each train contained 60 bunches. The bunch spacing was 4 RF buckets.

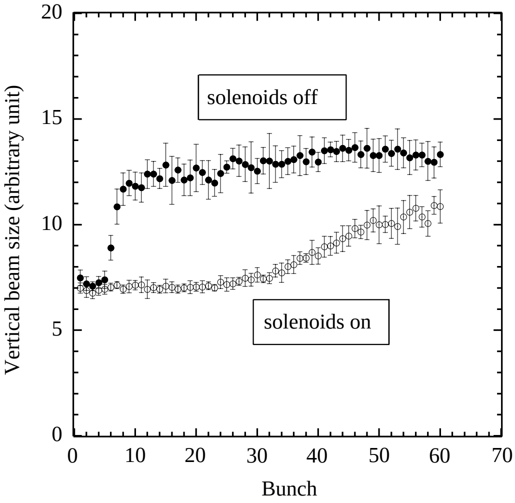

Fig. 7. Vertical beam size as a function of the beam current. In the measurement, two trains were injected on opposite sides of the ring. Each train contained 60 bunches. The bunch spacing was 4 RF buckets.

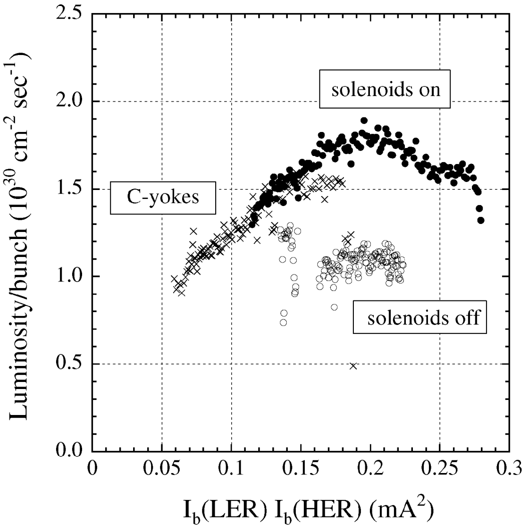

Fig. 8. Luminosity per bunch with and without the solenoids. The horizontal axis is the product of the bunch currents of the LER and HER. The data with the C-yokes is also shown. Bunch fill-pattern was that used during physics running. The number of bunches and the bunch spacing were 1153 and 4 RF buckets, respectively.

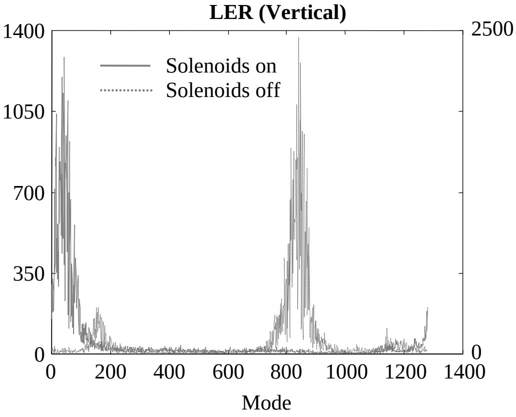

Fig. 9. Vertical mode spectrum with and without the solenoid magnets in the LER.

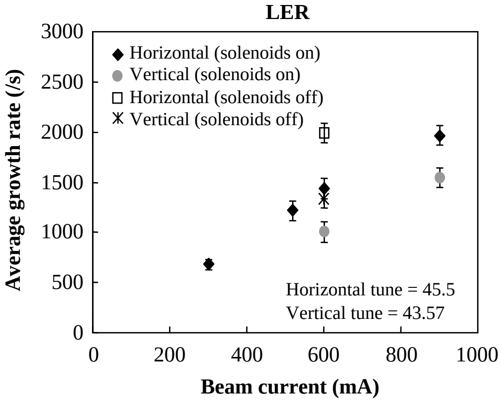

Fig. 10. Average growth rate in the LER.

bunch spacings to achieve higher luminosity in KEKB.

In measurements of the TCBI, only one train consisting of 1153 bunches separated by 4 RF-bucket spacing was stored in the HER or the LER. A train-gap of continuous 512 RF buckets unoccupied by a beam was introduced. The dipole oscillation of every bunch was recorded turn by turn, with a bunch oscillation recorder up to 4096 turns after turning off the transverse bunch-by-bunch feedback system. A Fourier analysis was applied to the oscillation of each bunch to extract the component of the betatron oscillation. Obtained Fourier components were processed by an inverse Fourier transform after correcting arrival times of the bunches at a beam position detector to obtain snapshot patterns of the oscillation. Mode spectrum of the coupled-bunch oscillation was obtained by applying a Fourier analysis to the snapshot patterns after padding zeros in the train gap.

Fig. 9 shows the mode spectra of the vertical plane of the LER with and without the solenoid magnets. In the horizontal plane, similar spectrum to the vertical one was obtained. It can be seen that the spectra of the excited modes with and without the solenoid fields are quite different from each other. The average growth rates of the bunch oscillation over the bunches in the LER are presented in Fig. 10. The observed growth rates are very high and are proportional to the beam current. At a beam current of 600 mA the growth rate was reduced by 38% horizontally and 34% vertically, when the solenoids were turned on. This suggests that the solenoid fields have removed a portion of the electron cloud that contributes to the amplitude growth of the bunch oscillations.

Fig. 11 shows the mode spectrum of the vertical plane in the HER. The mode spectrum calculated

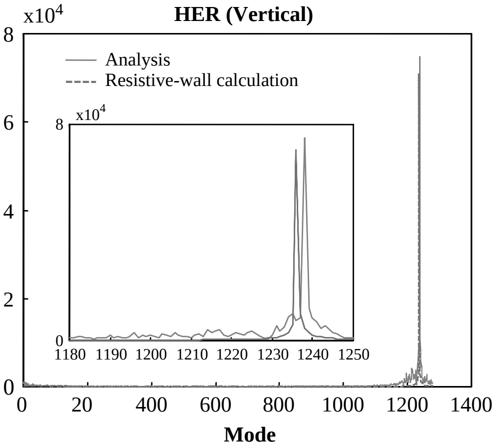

Fig. 11. Vertical mode spectrum in the HER.

with a resistive-wall wake is also shown in the figure. The calculated peak position appears near the observed peak, but the two do not exactly coincide. The measured growth rate at 700 mA is about three times higher than the calculated one. In the horizontal plane characteristics similar to that in the vertical plane were observed for both the mode spectrum and the growth rate. More studies are needed to conclude that the instability is caused by the resistive-wall wakefields.

4.3. Fast beam-ion instability

The fast beam-ion instability (FBII) was studied in the HER [10]. In the experiment, eight bunch-trains, each of which contained 120 bunches with a 4 RF-bucket spacing, were stored in the HER. The gap between neighboring trains was 80 RF buckets. The beam current was 240 mA and the average vacuum pressure was 1.4×10^{-7} Pa. The vertical dipole oscillations of the bunches were recorded turn by turn by a bunch oscillation recorder up to 4096 turns after turning off the transverse bunch-by-bunch feedback system.

A Singular Value Decomposition (SVD) method was applied to analyze the data. In the method, the data were arranged in a matrix Y with K rows by M columns, where K is the total number of turns and M is the total number of bunches in a train. Then, Y was decomposed as

$$Y = U^{\mathrm{T}} W V.$$

The row vectors of U and V represent the time patterns and spatial patterns of the oscillation, respectively.

In the measurement the spatial pattern of the largest singular value which appears in the diagonal element of W showed a snake-like bunch oscillation, i.e., the oscillation amplitudes grew from the head to the tail of the train, as shown in Fig. 12. The wavelength of the spatial pattern was consistent with that obtained assuming the CO ions were responsible for the instability. To see the effect of the vertical beam size on the instability, the vertical beam size was changed by controlling the vertical dispersion. The wavelength of the oscillation was changed as predicted by the FBII theory, as shown in Fig. 13. A (quasi-exponential) growth time of the oscillation was evaluated from the time pattern of the oscillation and was estimated to be 0.15 ms, after subtracting the head–tail damping time which was estimated from the current-dependent tune shift. An analytical estimation of the growth time of the FBII is 0.48 ms, which is not far from the measured growth time.

4.4. Transverse mode-coupling instability

A transverse mode-coupling instability was observed in the vertical plane in the LER. Fig. 14 shows two betatron modes, $m = 0$ and -1, observed on a spectrum analyzer. As the bunch

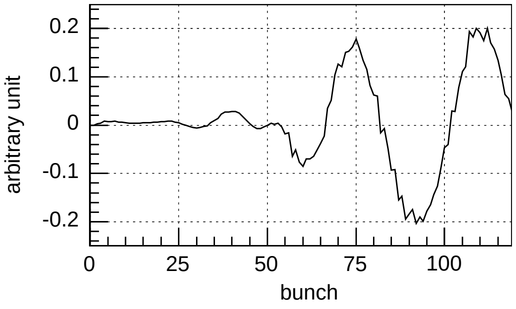

Fig. 12. Oscillation amplitude along a bunch train. Left is a head of the train.

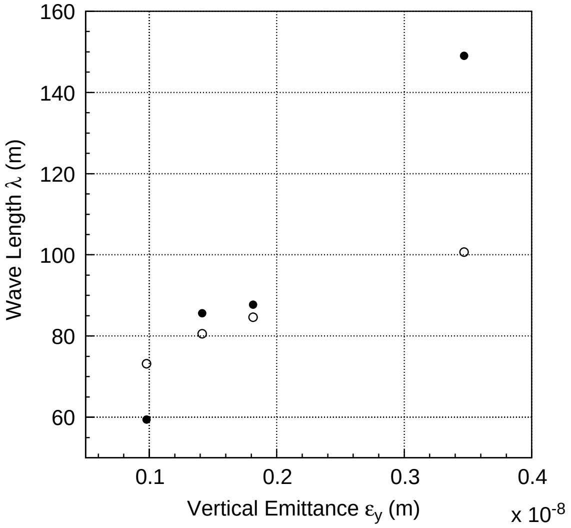

Fig. 13. Wavelength of the oscillation as a function of the vertical emittance. The closed circles show the measurements; the open circles show calculations by an analytic formula [10] assuming CO ions.

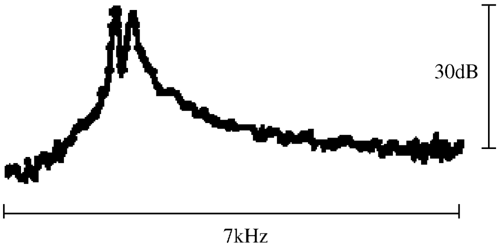

Fig. 14. Beam spectrum observed with a spectrum analyzer. The right and left peaks correspond to the $m = -1$ and 0 betatron modes, respectively.

current increased, the frequency of the $m = 0$ mode decreased, while that of the $m = -1$ mode almost did not change. When the bunch current exceeded the threshold bunch-current, the beam was lost. In Fig. 15, the threshold bunch-current at which the beam was lost is plotted as a function of the synchrotron tune. The threshold current is proportional to the synchrotron tune, as is predicted by the theory of the transverse mode-coupling instability. From the slope of the fitted line, the effective transverse impedance was estimated to be 133 kΩ/m, assuming a bunch length of 7 mm. It was found that the main part of the effective transverse impedance came from the vertical collimators, because the impedance was reduced to 46 kΩ/m after the collimators were fully opened.

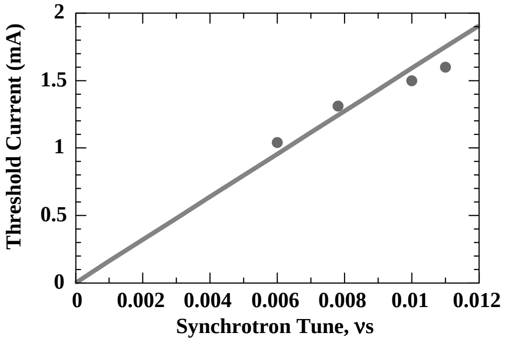

Fig. 15. Threshold bunch current of beam loss vs. synchrotron tune.

5. Beam–beam effects

5.1. Introductory remarks

In this section a brief summary of the beam–beam effects observed in KEKB is given. Like in other conventional e^+e^- colliders, also in KEKB the beam–beam effects impose a strict restriction on its luminosity. However, the nature of the effects in KEKB is much more complicated, or richer, compared with those in the conventional machines. This complication comes mainly from its unique characteristics of an asymmetric (double ring) collider. Since KEKB is an asymmetric collider, the beta functions at the IP, the beam currents and even the emittances can be chosen independently for the two beams. Although energy transparency conditions were proposed in the design phase of the machine, the present KEKB parameters heavily break these conditions. It is believed that the necessity of this break originates from the electron-cloud instability in the positron ring. The beta functions at the IP, the beam currents, bunch spacing and the horizontal and vertical emittances have been determined by a trial-and-error method so that, the luminosity should be maximized. The meanings of all these remarks are as follows: (1) Once the energy transparency conditions are broken for some reason, the dimensions of the parameter space to be optimized become huge, and a search for an optimum set of the parameters becomes a very time-consuming work. (2) The origin of the energy transparency breaking seems to come from a difference in the particle species. Unlike conventional single-ring colliders, the mechanism of an (averaged) neutralization of space charge of the two beams does not work in double-ring colliders, and the electron cloud or fast ion instability could be an issue. These instabilities can become even more serious due to a requirement of very high beam currents in the factory machines. When a beam–beam blowup coexists with the single-beam blowup of the LER due to the electron-cloud instability, the beam performance should be optimized considering the two effect. In addition, in some situations it is not easy to distinguish the beam blowup from the two effect. This sometimes causes some confusion in understanding the nature of the beam blowup. Also, in some situations, we might have to consider a synergistic effect of the two processes, although there has been no direct evidence for this.

Another complication concerning a double-ring collider is that machine tuning concerning geometrical overlapping of the two beams at the IP, such as orbits, waist points of the beta functions and x–y coupling, is important. Any slippage from the optimum values of these parameters can cause not only a geometrical loss in the luminosity, but also an additional beam–beam blowup. In KEKB, during daily machine operation, an orbit feedback system, called "iBump feedback", is always active so as to maintain the optimum relative orbit, as described in Section 5.3. In addition, as we will describe in Section 5.4, we have another feedback system, called "iSize feedback", in order to maximize the luminosity by controlling the vertical emittance of the stronger beam (usually the HER). We need careful tuning on these parameters, including the feedback systems mentioned above, for maximizing the luminosity. The beam–beam performance described in this section is that based on these adjustments.

Another unique characteristic of KEKB is a finite (horizontal) crossing angle of ± 11 mrad. It seems that there is no serious problems originating from the crossing angle so far, although we have not yet performed a systematic study on this issue.

5.2. Beam–beam performance

5.2.1. Basic features of the KEKB machine parameters

The beam–beam performance is closely related to the choice of other machine parameters. Before describing the beam–beam performance, we should quickly review the basic parameters of KEKB. Table 1 lists a parameter list of KEKB at the record peak luminosity.

At present, each of the KEKB rings is filled with a beam at every 4th RF bucket. In the original design [1], the number of bunches was assumed to be around 5000, which means that every RF bucket is filled with a beam (except for a gap which is necessary to wait for the abort kicker to be ready). When the number of bunches is increased from the every 4th RF-bucket case, the specific luminosity is decreased. Although we tried longer bunch spacings, the 4 RF-bucket spacing (~ 8 ns) is the best choice. The other parameters are chosen under this restriction of the bunch spacing.

It is notable that the bunch currents of the present KEKB are much higher compared with the design values, particularly in the HER. This is a consequence of the bunch spacing restriction. To compensate this unusually high bunch current to some extent, the horizontal emittance of the HER is enlarged compared with the design value. On the other hand, the LER bunch current is not so high compared with the design current as that of the HER. The luminosity does not increase even with higher LER beam current. The horizontal and vertical beta functions at the IP has been determined by a trial and error method. The vertical beta functions are much lower than the design values. The present working points of KEKB are determined mainly through optimization of the beam–beam effects as is described below.

5.2.2. Beam–beam parameters and specific luminosity

To assess beam–beam performance of a collider, a common way is to see the specific luminosity and the beam–beam parameters. The specific luminosity is defined as the luminosity divided by the number of bunches and also divided by the product of bunch-currents of the two beams. One thing that one should note here is that these parameters are not necessarily determined only by beam–beam effects. They can be affected by other beam-blowup mechanisms, such as the electron-cloud instability.

In Figs. 16 and 17, the specific luminosity is shown as a function of a square root of a bunch-current product and the LER total beam current. The specific luminosity should be constant, if the beam sizes would not change. Thus thee slopes in the figures mean that the sizes continuously shrink as the beam currents decrease in the course of the fills. The figures show comparisons of the specific luminosity with a 3 RF-bucket spacing to that with the 4 RF-bucket spacing.

The data in Fig. 16 were taken before the summer shutdown in 2001 and those in Fig. 17 were after the shutdown. During the shutdown, additional solenoid coils of about 500 m in total were wound in the LER. In the left graph of Fig. 16, the specific luminosity with the 3-bucket spacing is much lower than that with the 4-bucket spacing. If the beam blowup was induced purely by the beam–beam effect, the two curves in these graphs should overlap. Therefore, the different behaviors of the two curves indicate that a beam-blowup mechanism other than the beam–beam effect plays a part in the blowup. Since the beam blowup is usually observed in the vertical direction of the LER beam, the electron-cloud instability is a first candidate for this mechanism.

However, even below the threshold beam current of this instability, the specific luminosity with the 3-bucket spacing is much lower than that with the 4-bucket spacing, and we cannot attribute this difference to the electron-cloud instability alone. We might have to consider a synergistic effect of the beam–beam effect and the electron-cloud instability. Recently, E.A. Perevedentsev et al. and K. Ohmi independently proposed a model in which a coherent beam–beam instability of the head–tail type could be induced by the beam–beam effect combined with some ring impedance [11,12]. This model might be applicable to the present case by regarding the electron cloud as the impedance source.

After the addition of the solenoid coils during the summer shutdown in 2001, the situation changed. As is seen in Fig. 17, the specific luminosity with the 3-bucket spacing is much

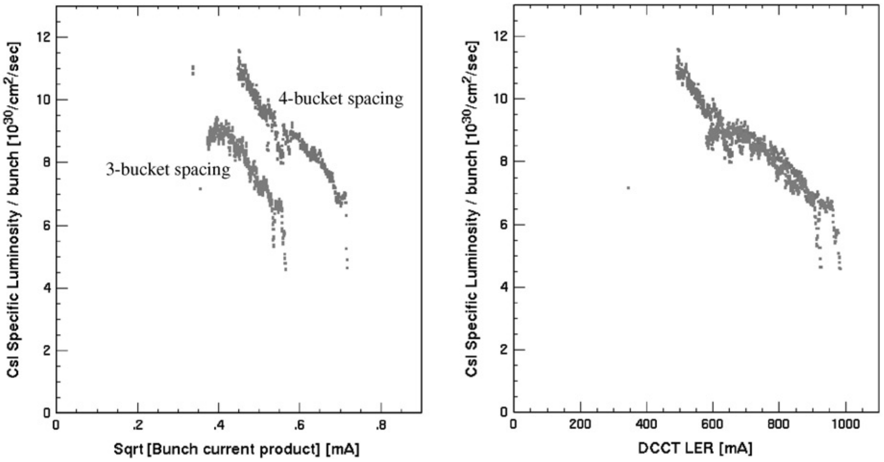

Fig. 16. A specific luminosity as function of a square root of the bunch current product and the LER total beam current. These data were taken on July 11 and 12 in 2001 (before the summer shutdown).

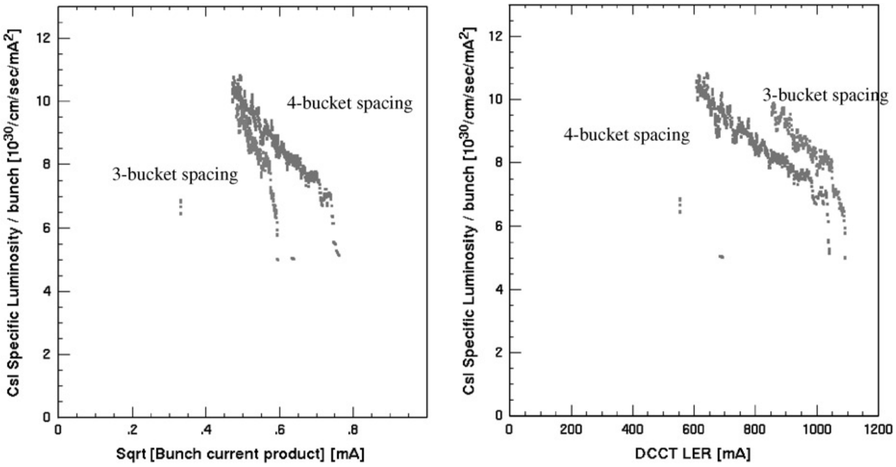

Fig. 17. A specific luminosity as function of a square root of the bunch current product and the LER total beam current. These data were taken on November 9 and 10 in 2001 (after the summer shutdown).

improved, although the improvement in that with the 4 bucket spacing is small. In the left graph of Fig. 17, the two curves meet at around the lowest beam current of the LER. Roughly speaking, the beam current (~900 mA) agrees with the threshold beam current of the electron-cloud instability after the addition of the solenoid coils. Therefore, in this case, it seems that difference in the specific luminosity with 3- and 4-bucket spacing could be explained by the electron-cloud instability.

A more fundamental question is that the origin of the steep slopes of the curves in Figs. 16 and 17. Since the continuous beam blowup during the fill seems quite unusual compared with conventional colliders, the origin of these beam-size enlargements has been controversial. There has been some suspicion that the beam blowup does not come from the beam–beam effect but from the electron-cloud instability. This doubt was likely to be supported by an observation that the beam blowup is mainly observed in the vertical direction of the LER. To distinguish these two effects, an experiment with longer bunch spacing of 24 RF buckets was done. With this bunch spacing, we observed no single beam blowup in the usual bunch current region. In this experiment, we observed the luminosity down to lower beam currents than the usual physics operation. The result is shown in Fig. 18. As shown in the figure, the specific luminosity with 24 bucket spacing is almost the same as that with 4 bucket spacing. This result indicates that the beam blowup in the beam current region of the usual physics run does not originate from the electron-cloud instability but from the beam–beam effect. This explanation is also supported by beam–beam simulations. In Fig. 19, results of the beam–beam simulations are also shown by using a strong–strong simulation code [13]. Although a quantitative agreement between the simulations and the experiments is not so good, the simulations reproduce the tendency of the beam current dependence of the specific luminosity. Fig. 19 also shows that the specific luminosity does not become constant even at a very low beam current and this is also supported by the simulation. As is described above, the bunch current of the present KEKB is much higher than that of the design. The beam currents during the usual physics operation seem to be well above the beam–beam limit.

The beam–beam parameters calculated from the luminosity at the record peak luminosity are already listed in Table 1. In the calculation, we assumed that the vertical beam sizes of the two beams are equal, since we use the iSize feedback system. It is also assumed that there is no beam–beam blowup in the horizontal direction, since we do not observe serious beam size blowup in the

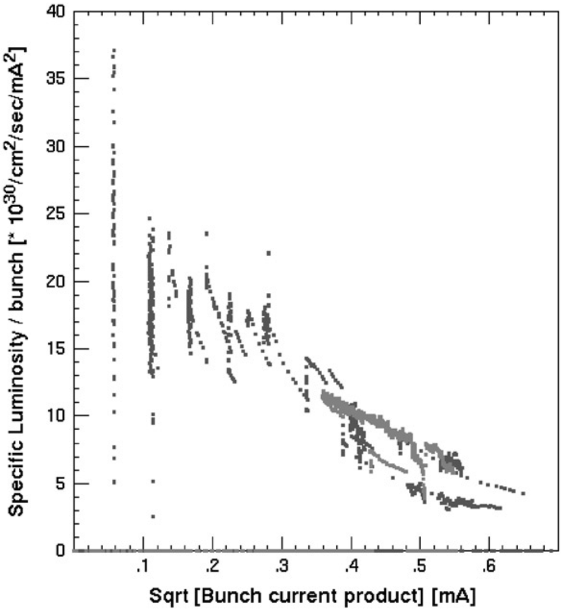

Fig. 18. A current dependence of the specific luminosity with different bunch spacing of 4 bucket (red) and 24 bucket (green). The specific luminosity in this figure is somewhat lower than that in Figs. 16 and 17. This is because the data in this figure are a bit old and there was some luminosity improvement after these data had been taken. These two data were taken on the same day (March 10, 2001).

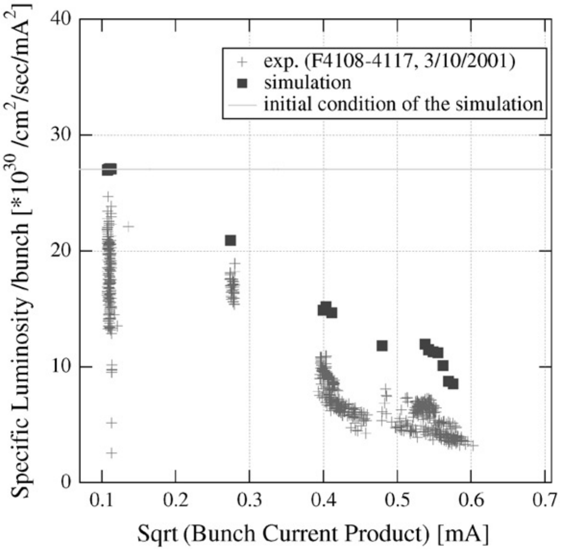

Fig. 19. A comparison of the measured specific luminosity with a 24-bucket bunch spacing to that from the beam–beam simulation using a strong–strong code.

horizontal direction. The “hourglass” effect from a finite bunch length and degradation of the beam–beam parameters due to a finite crossing angle are also considered. As for the bunch length, 7 mm is assumed. As is seen in Table 1, the vertical beam–beam parameter of the HER is notably low compared with the design value. This is also explained by the single beam blowup of the LER from the electron-cloud instability.

5.2.3. Dynamic β and dynamic emittance

Another feature of the KEKB parameters is that the working points are close to the half-integer resonance, as is shown in Table 1. Particularly, the horizontal tunes are very near to the resonance. In this situation of importance is the change of the beta function and the emittance due to the beam–beam force (dynamic-beta and dynamic-emittance). These effects have been studied using the SAD code. The change in emittance is numerically calculated taking only the linear part of the beam–beam kick into account. Fig. 20 shows a result of the calculation. In the figure, the beta function of the LER at the IP and the horizontal emittance are depicted as functions of the (nominal) horizontal beam–beam parameter. Also shown in the figure is the beta function which is evaluated by an analytic calculation. The beta function can be calculated by estimating a change of an one-turn transfer matrix with the beam–beam kick. The analytic calculation well agrees with that from the SAD code. As is seen in the figure, the horizontal beta function at the IP drastically shrinks with the horizontal tune of 45.51 and the emittance is enlarged. As a result of these changes, the horizontal beam size at the IP decreases to a some extent and the (real) horizontal beam–beam tune shift decreases.

What one should note here is that a change in the beam size in one beam due to the beam–beam effect causes additional dynamic changes in the beta function and emittance of the other beam. Therefore, the resultant values of the beta function and the emittance should be derived consistently for the two beams. By using the parameters in Table 1 with which the record peak luminosity was

Table 3
Comparison of the beam–beam parameters with 4 bucket spacing at the record peak luminosity on October 31 2001

	Spacing	Measurement	Real tune shift	Design
ξ_x/ξ_y (LER)	4 buckets	0.073/0.047	0.017/0.042	0.039/0.052
ξ_x/ξ_y (HER)	4 buckets	0.061/0.035	0.020/0.030	0.039/0.052

Real tune shifts which include the dynamic beta and dynamic emittance effects are also shown. The design beam–beam parameters are also listed.

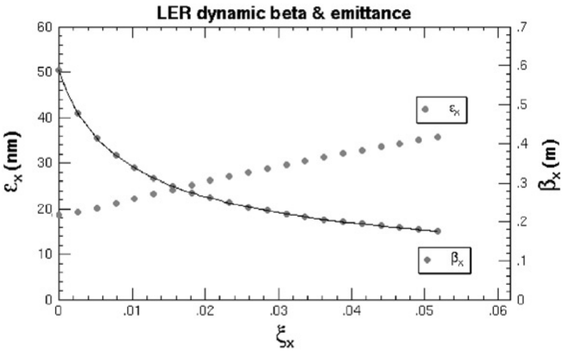

Fig. 20. Calculations of the dynamic beta and dynamic emittance effects with a horizontal tune of 45.51 as function of the (nominal) horizontal beam–beam parameter. The calculation was done by using the SAD code. The solid line shows a beta calculation from an analytical calculation using a simple one-turn transfer matrix.

achieved, these parameters were calculated. The horizontal beta functions at the IP of the LER and HER change from 59 cm (LER) and 63 cm (HER) to 9.57 cm (LER) and 15.7 cm (HER). The horizontal emittances of the LER and HER also change due to the beam–beam effect from 18 nm (LER) and 24 nm (HER) to 65.6 nm (LER) and 51.2 nm (HER). In Table 3, the real beam–beam tune shifts including the dynamic beta and dynamic emittance effects are shown. As can be seen in the table, the horizontal tune shifts are much smaller than the beam–beam parameters. It seems that the unusually high (horizontal) beam–beam parameters in KEKB are achievable due to these effects. In KEKB, there is a tendency that the horizontal tune closer to the half-integer resonance brings a higher luminosity. This tendency also seems to be explained by the dynamic beta and dynamic emittance effects.

5.2.4. Tune survey

It is commonly known that the beam–beam performance is strongly dependent on the choice of the working points. KEKB is not an exception. Since the design phase of KEKB, an enormous amount of effort has been devoted to searches for better working points in both simulations and experiments on the real machine. In the design phase, the large-scale simulations with a strong–strong code were not realistic due to the restriction of the computing power. The design tunes were determined by using a strong–weak simulation code [1]. Although there was no significant difference between just above the integer resonance and just above the half-integer resonance, as for the vertical tune, the vertical tune just above the integer was chosen for the design tune for the purpose of avoiding effects of the *x–y* coupling. The recent quickly developing computing power has enabled us to make a tune survey with a strong–strong code, although the survey is still a time-consuming task, even today. The recent beam–beam simulations using the strong–strong code predicted that the vertical tune just above the half-integer gives a higher luminosity than that above the integer [14]. A comparison of the simulated luminosity for these two tune regions is shown in Fig. 21. As seen in the figure, the tune above the half-integer gives a higher luminosity. Following this prediction, we changed the vertical tunes of both rings from just above the integer to just above the half-integer in February 2001. This change in tunes has brought about not only a jump in the luminosity, but also improved stability of the machine operation through more stable beam orbits. The tunes shown in Table 1 were obtained by a trial and error method in a long-term machine operation.

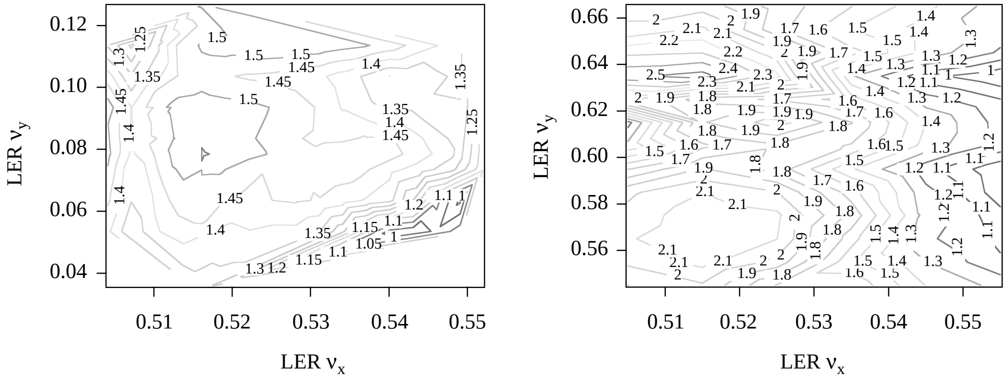

Fig. 21. Results of tune surveys in two different tune regions by using a strong–strong tracking program. The luminosity in the figure is that of a pair of bunches in unit of 10^{30} cm^{-2} s^{-1}. In the tracking, an effect of a finite bunch length was taken into account by slicing the bunches in the longitudinal direction. The number of slices was 5. The tunes of the HER were kept constant; $(\nu_x, \nu_y) = (0.5136, 0.6344)$ in the right figure and $(\nu_x, \nu_y) = (0.5250, 0.1350)$ in the left figure. In the right figure, a luminosity peak near the third integer resonance of the vertical tune is seen. Although we tried this tune region in the actual beam operation, we could not obtain higher luminosity than the present working point. It turned out that this luminosity peak in the simulation can easily disappear with small errors such as a 0.1 mrad vertical crossing angle.

5.3. Orbit feedback system around the IP

The orbit feedback system specially prepared near the IP, called "iBump", consists of 12 dipole correction magnets, 4 for horizontal and 8 for vertical orbital corrections. The magnets are located in the straight section on the left and right sides of the IP in the HER. These magnets are dedicated to the iBump feedback system and are used to create bumps at the IP to maintain collisions. The bipolar power supplies are controlled by a CAMAC DAC and monitored by a CAMAC ADC. This feedback system controls only the HER orbit. The global orbit feedback for the HER and the LER is taken care of by another task, called "CCC", which was described in Section 3.3. Handshaking between the iBump feedback and CCC is done so that the CCC task does not interfere with the bumps created by iBump.

5.3.1. Feedback parameters

The beam position for the feedback is monitored by the BPMs on the superconducting quadrupole magnet (QCS). With the QCS BPMs in the HER located at positions A and B and the LER BPMs at C and D, the beam positions at A and B are written as

$$x_{\rm e}^{\rm A} = m_{11}^{\rm A} x_{\rm e}^{*} + m_{12}^{\rm A} x_{\rm e}^{\prime * {\rm a}} \tag{4}$$

$$x_{\rm e}^{\rm B} = m_{11}^{\rm B} x_{\rm e}^{*} + m_{12}^{\rm B} x_{\rm e}^{\prime * {\rm b}} \tag{5}$$

where $m^{\rm A}$ and $m^{\rm B}$ are the transfer matrix from the IP to A and the inverse of the transfer matrix from B to the IP, respectively. The subscript e represents the e$^-$ beam. We have equations similar to these for the positron beam. The superscripts a and b correspond to after and before a collision. The asterisks denote the values at the IP and the primes indicate angles. Using the transfer matrices, the horizontal beam–beam kick that the e$^-$ beam receives is written as

$$\begin{aligned}\Delta x_{\rm e}^{\prime *} &= x_{\rm e}^{\prime * {\rm a}} - x_{\rm e}^{\prime * {\rm b}} \\ &= \left(\frac{x_{\rm e}^{\rm A}}{m_{12}^{\rm A}} - \frac{x_{\rm e}^{\rm B}}{m_{12}^{\rm B}}\right) - \left(\frac{m_{11}^{\rm A}}{m_{12}^{\rm A}} - \frac{m_{11}^{\rm B}}{m_{12}^{\rm B}}\right) x_{\rm e}^{*}.\end{aligned} \tag{6}$$

Similarly, the e$^+$ beam receives the following horizontal kick:

$$\begin{aligned}\Delta x_{\rm p}^{\prime *} &= x_{\rm p}^{\prime * {\rm a}} - x_{\rm p}^{\prime * {\rm b}} \\ &= \left(\frac{x_{\rm p}^{\rm C}}{m_{12}^{\rm C}} - \frac{x_{\rm p}^{\rm D}}{m_{12}^{\rm D}}\right) - \left(\frac{m_{11}^{\rm C}}{m_{12}^{\rm C}} - \frac{m_{11}^{\rm D}}{m_{12}^{\rm D}}\right) x_{\rm p}^{*}.\end{aligned} \tag{7}$$

From Eqs. (6) and (7), a new parameter $\Delta x'^{*}_{x\mathrm{can}}$, called the "canonical horizontal kick" is obtained as follows:

$$\Delta x'^{*}_{x\mathrm{can}} \equiv \frac{\dfrac{x_{\mathrm{e}}^{\mathrm{A}}}{m_{12}^{\mathrm{A}}} - \dfrac{x_{\mathrm{e}}^{\mathrm{B}}}{m_{12}^{\mathrm{B}}}}{\dfrac{m_{11}^{\mathrm{A}}}{m_{12}^{\mathrm{A}}} - \dfrac{m_{11}^{\mathrm{B}}}{m_{12}^{\mathrm{B}}}} - \frac{\dfrac{x_{\mathrm{p}}^{\mathrm{C}}}{m_{12}^{\mathrm{C}}} - \dfrac{x_{\mathrm{p}}^{\mathrm{D}}}{m_{12}^{\mathrm{D}}}}{\dfrac{m_{11}^{\mathrm{C}}}{m_{12}^{\mathrm{C}}} - \dfrac{m_{11}^{\mathrm{D}}}{m_{12}^{\mathrm{D}}}}$$

$$= \frac{\Delta x'^{*}_{\mathrm{e}}}{\dfrac{m_{11}^{\mathrm{A}}}{m_{12}^{\mathrm{A}}} - \dfrac{m_{11}^{\mathrm{B}}}{m_{12}^{\mathrm{B}}}} - \frac{\Delta x'^{*}_{\mathrm{p}}}{\dfrac{m_{11}^{\mathrm{C}}}{m_{12}^{\mathrm{C}}} - \dfrac{m_{11}^{\mathrm{D}}}{m_{12}^{\mathrm{D}}}} + \Delta x^{*} \tag{8}$$

$$= \left(\frac{-k_{\mathrm{e}}}{m_{\mathrm{e}}} + \frac{-k_{\mathrm{p}}}{m_{\mathrm{p}}} + 1\right)\Delta x^{*} \tag{9}$$

where

$$\Delta x'^{*}_{\mathrm{e}} = -k_{\mathrm{e}}\Delta x^{*} \tag{10}$$

$$\Delta x'^{*}_{\mathrm{p}} = k_{\mathrm{p}}\Delta x^{*} \tag{11}$$

$$m_{\mathrm{e}} = \frac{1}{\dfrac{m_{11}^{\mathrm{A}}}{m_{12}^{\mathrm{A}}} - \dfrac{m_{11}^{\mathrm{B}}}{m_{12}^{\mathrm{B}}}} \tag{12}$$

$$m_{\mathrm{p}} = \frac{1}{\dfrac{m_{11}^{\mathrm{C}}}{m_{12}^{\mathrm{C}}} - \dfrac{m_{11}^{\mathrm{D}}}{m_{12}^{\mathrm{D}}}} \tag{13}$$

and

$$\Delta x^{*} \equiv x_{\mathrm{e}}^{*} - x_{\mathrm{p}}^{*}. \tag{14}$$

In the expressions above, we treat only the linear part of the beam–beam force. The vertical canonical kick can be expressed similarly. The canonical parameters are functions of the difference of the two beam positions Δx^{*} and are therefore good parameters to use for collision feedback. The parameters m_{e} and m_{p} in Eq. (9) are constants calculated from the transfer matrices, while k_{e} and k_{p} are functions of the beam–beam parameters and depend on the beam current and the beam sizes. The canonical crossing angle between the two beams can also be defined. The following equation gives the horizontal canonical crossing angle $\theta_{x\mathrm{can}}$:

$$\theta_{x\mathrm{can}} \equiv \frac{\dfrac{x_{\mathrm{e}}^{\mathrm{A}}}{m_{12}^{\mathrm{A}}} + \dfrac{x_{\mathrm{e}}^{\mathrm{B}}}{m_{12}^{\mathrm{B}}}}{\dfrac{m_{11}^{\mathrm{A}}}{m_{12}^{\mathrm{A}}} + \dfrac{m_{11}^{\mathrm{B}}}{m_{12}^{\mathrm{B}}}} - \frac{\dfrac{x_{\mathrm{p}}^{\mathrm{C}}}{m_{12}^{\mathrm{C}}} + \dfrac{x_{\mathrm{p}}^{\mathrm{D}}}{m_{12}^{\mathrm{D}}}}{\dfrac{m_{11}^{\mathrm{C}}}{m_{12}^{\mathrm{C}}} + \dfrac{m_{11}^{\mathrm{D}}}{m_{12}^{\mathrm{D}}}}. \tag{15}$$

The vertical canonical crossing angle is obtained by replacing m_{11}^{A}, m_{11}^{B}, m_{12}^{A}, m_{12}^{B} in Eq. (15) with m_{33}^{A}, m_{33}^{B}, m_{34}^{A}, m_{34}^{B} and using the vertical positions from the BPMs.

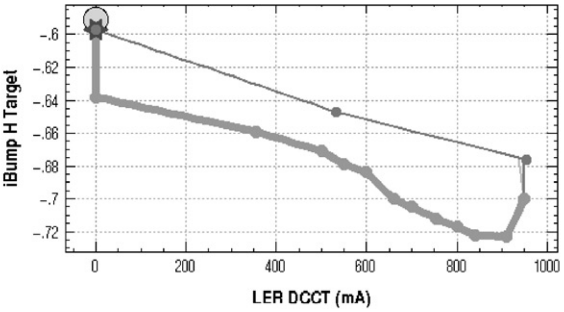

Fig. 22. Example of a diagram for the target value for $\Delta x'^{*}_{x\mathrm{can}}$. The target is programmed to change as a function of the LER current during a fill.

The idea of the iBump feedback is to maintain the optimum collision condition by keeping the canonical kicks and crossing angles at certain target values. The rough target values are found by a deflection scan, which is performed occasionally at the beginning of a fill after machine maintenance. The iBump feedback system does not search for the optimum target by itself. Fine tuning of the vertical target values is performed by shift operators during a fill by monitoring the luminosity. It is found empirically that the target for $\Delta x'^{*}_{x\mathrm{can}}$ needs to be changed more frequently than that for $\Delta x'^{*}_{y\mathrm{can}}$. It is currently changed by a program which sets the target as a function of the LER current according to a diagram. An example of the diagram is shown in Fig. 22. This diagram can be changed by the operator.

5.3.2. Feedback algorithm

The feedback quantity for the nth iteration, x_n, can be expressed by a linear combination of the past N ($\equiv$ Dimension) data points as [20]

$$x_n = \sum_{k=1}^{N} c_k x_{n-k}. \tag{16}$$

The previous feedback quantities, x_{n-1}, x_{n-2}, etc. can be expressed similarly and the following M ($\equiv$ Depth) sets of linear equations are obtained

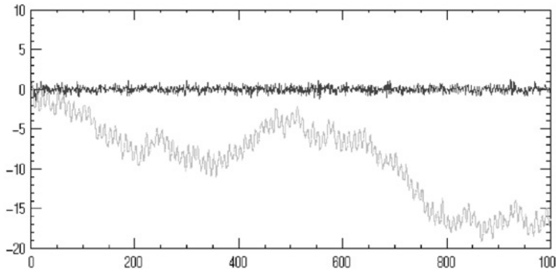

Fig. 23. Feedback simulation with a gain factor of 1. The thin line shows the input to the feedback (randomized periodic function plus randomized drift function). The dark line shows the result after a feedback correction.

using a set of coefficients, c_k

$$\text{Depth}\Downarrow\begin{pmatrix} x_{n-1} & x_{n-2} & x_{n-3} & x_{n-4} & x_{n-5} & x_{n-6} \\ x_{n-2} & x_{n-3} & x_{n-4} & x_{n-5} & x_{n-6} & x_{n-7} \\ x_{n-3} & x_{n-4} & x_{n-5} & x_{n-6} & x_{n-7} & x_{n-8} \\ \vdots & \vdots & \vdots & \vdots & \vdots & \vdots \end{pmatrix} \times \begin{pmatrix} c_1 \\ c_2 \\ c_3 \\ c_4 \\ c_5 \\ c_6 \end{pmatrix} = \begin{pmatrix} x_n \\ x_{n-1} \\ x_{n-2} \\ \vdots \\ \vdots \\ \vdots \end{pmatrix}. \tag{17}$$

The coefficients c_k can be solved for as long as Depth$\geqslant$Dimension. N and M are chosen empirically to be 6 and 48, respectively, for the current operation. Fig. 23 shows a simulation of this feedback scheme in operation. Using c_k, the next feedback quantity x_{n+1} is calculated. In an actual operation, the calculation result is multiplied by a gain factor, which is determined empirically.

5.3.3. *Feedback performance*

The feedback speed is limited by the BPM readout time. The iBump feedback cycle times are 2 and 3 s for the vertical and horizontal plane, nominally. The ranges of the bump heights are ±200 and ±150 μm for horizontal and vertical offsets, respectively, in order to protect the Belle detector from being irradiated. The effect of a horizontal bump on the vertical orbit is nonnegligible due to x–y coupling. This coupling effect is taken care of by creating an extra vertical bump, which cancels out the coupling.

5.3.4. *Example*

The plots in Fig. 24 show the height of the bump created by the iBump feedback system during Fill 5931. The collision feedback is turned on during injection. Once the injection finishes, the horizontal bump height changes by more than 100 μm, while the vertical bump changes by several μm over the course of the fill. Fig. 25 shows $\Delta x'^{*}_{x\mathrm{can}}$ and $\Delta x'^{*}_{y\mathrm{can}}$ for the same fill. The feedback target value for $\Delta x'^{*}_{y\mathrm{can}}$ was kept constant, while that for $\Delta x'^{*}_{x\mathrm{can}}$ was changed according to a diagram. The fluctuations can be translated into the fluctuation in the difference of the relative beam positions Δx^{*} if the beam–beam parameters (see elsewhere in this paper for the calculation method) in Table 1 are used.

The peak-to-peak fluctuation around the target was estimated to be 0.4 and 20 μm for vertical and horizontal beam positions, respectively. These numbers can be compared with the beam sizes measured by the synchrotron-radiation monitor (SRM) [4]. The measured vertical and horizontal beam sizes at the IP at high current are 4.5 and 120 μm, respectively, at the beginning of a fill.

In order to see the effect of iBump, it was deactivated for $\Delta x'^{*}_{y\mathrm{can}}$ during one fill. The feedback for the other parameters was kept activated. Fig. 26 shows that the luminosity dropped by 20% when the feedback was turned off at around 3 min after midnight. The feedback was turned back on after 2 min and the luminosity recovered soon after.

5.3.5. *Summary*

Once a good collision condition is found, it is maintained by the iBump feedback system. The fluctuation of the difference of relative beam positions is typically much smaller than the beam sizes. The feedback targets are currently found by the operators through adiabatic tuning. We would like to automate as many processes as possible in the near future. Monitoring the beam positions by the OctoPos [15] BPMs, which are located closer

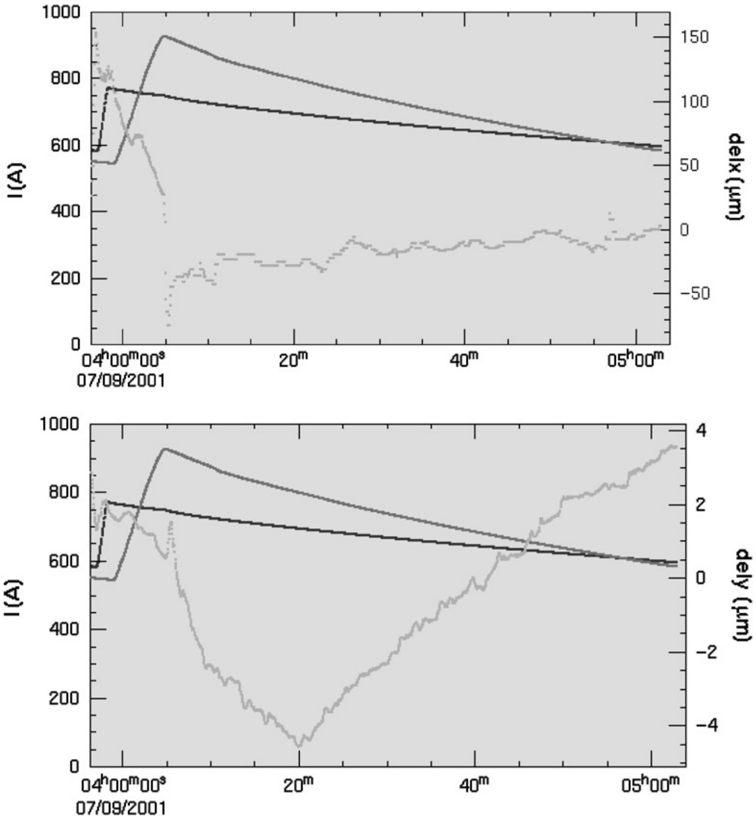

Fig. 24. Horizontal and vertical bump size created by iBump feedback during a typical Fill 5931. The HER and LER currents are also shown in darker lines.

to the IP than the QCS BPMs, is being considered. Speeding up of the feedback system may be needed.

5.4. *Beam-size feedback system*

5.4.1. *Motivation of the beam-size control*

In KEKB, a blowup of the LER vertical beam-size is one of the most severe obstacles for increasing the luminosity. Two processes are supposed to cause this beam blowup. One is a single-beam blowup [16] induced by the electron cloud (as discussed in Section 4), and the other is that due to the beam–beam effect, which we have already explained in Section 5. Although we sometimes observe a blowup also in the horizontal plane, here we discuss only the vertical one.

From the beam–beam point of view, there are two reasons why the LER beam is weaker, both of which come from the electron-cloud beam blowup. One is that the present operating beam currents of KEKB heavily breaks the so-called the energy-transparency condition; the effective HER beam current is much higher than that of the LER, if we consider the energy difference of the two beams. This is because the higher HER beam current usually brings the higher luminosity whereas the higher LER beam current is less effective for increasing the luminosity due to the electron-cloud blowup. The other reason is that the LER vertical beam size of collision is larger than that of the HER due to the electron-cloud effect. Because of this beam size difference, particles in the LER feel a nonlinear beam–beam force more likely than

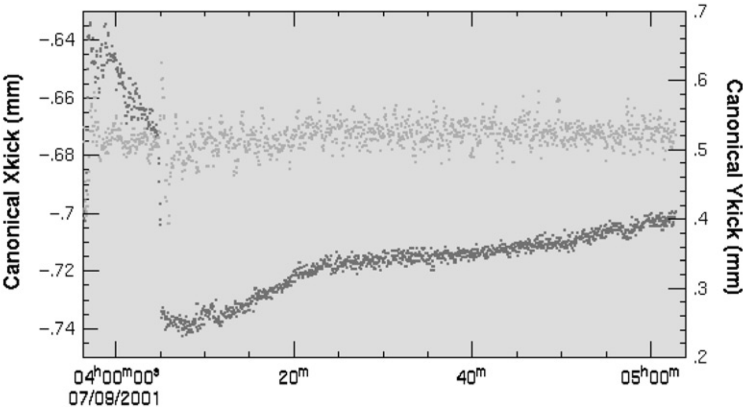

Fig. 25. $\Delta x'^{*}_{x\mathrm{can}}$(dark dots) and $\Delta x'^{*}_{y\mathrm{can}}$(thin dots) for Fill 5931 are shown. The vertical target was kept constant while the horizontal target was changed during the fill. The global trend of $\Delta x'^{*}_{x\mathrm{can}}$ is the result of the target change.

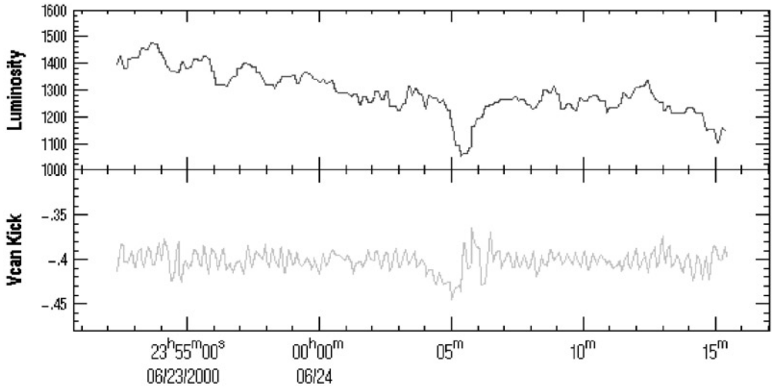

Fig. 26. Luminosity and $\Delta x'^{*}_{y\mathrm{can}}$ plotted against time. The feedback for $\Delta x'^{*}_{y\mathrm{can}}$ was turned off at 0:03 and luminosity drop followed.

those in the HER. This enhances the LER beam–beam blowup.

We empirically know that a higher luminosity is obtained when the blowing up of the LER vertical beam size caused by beam–beam effect is suppressed by making the HER beam larger intentionally. We found that the luminosity is very sensitive to the ratio of beam sizes, $\sigma_y^{\mathrm{LER}}/\sigma_y^{\mathrm{HER}}$. We constructed a feedback to keep the vertical beam size ratio to an optimum target value that is obtained empirically. In this section the feedback system which is used for the actual beam operation, called “iSize” feedback system is described.

5.4.2. Beam size control in the HER

In KEKB, the noninterleaved sextupole scheme is adopted for a chromaticity correction, and many pairs of sextupole magnets are installed in the arc section. At one of the strongest sextupole pairs in the HER, an anti-symmetric bump is made by exciting three dipole correction-magnets near them. This bump converts the horizontal dispersion to the vertical, which leaks out around the whole of the ring. On the other hand, the created horizontal–vertical coupling is closed in the bump and never leaks out. By this dispersion, the vertical emittance is enlarged and the HER beam size can be made larger. The emittance is a parabolic function of the iSize bump height. The iSize bump heights in the actual operation are mainly between 0 and 2 mm, which corresponds to an emittance of up to about 0.8 nm. These calculations are performed with the "SAD" code [3] in which a lattice for the current operations is used [17].

5.4.3. iSize feedback

The feedback routine uses a ratio $\sigma_y^{\mathrm{LER}}/\sigma_y^{\mathrm{HER}}$ as an input parameter. The aim of the feedback is to keep this ratio around the target value. The beam sizes are measured by synchrotron radiation monitors (SRMs) [18], which are located at the arc section of both rings. The SRMs can take data at about 5 Hz, and every five successive data are averaged. The measured beam sizes are converted to those at the interaction point by multiplying the measured beam size by a factor corresponding to square root of the beta-function ratio. The iSize feedback obtains a value for the beam size of each ring at about 1 Hz. Calibrations for absolute values of the beam sizes are presently under study. Based on the ratio, a bump height is determined.

Fig. 27 is an example of the control panel of the iSize feedback. The lower-right graph shows a trend of the measured vertical beam size of the HER as a function of the bump height. The blue line in the figure shows a hyperbolic curve fit with the plots, and the red line indicates the target value for σ_y^{HER}, which is calculated σ_y^{LER} divided by the target ratio. The bump height to be set is obtained as an intersection point of these two lines. Actual change in the bump height is reduced by multiplying a factor, which is necessary for stabilizing the feedback action. Typically, this factor is chosen to be about 0.01. The bumps are made by the dedicated dipole magnets exclusively used for the iSize controllers.

Trend graphs of the parameters used for the iSize feedback during 1 day are shown in Fig. 27. The beam currents were about 740 and 580 mA for the HER and LER, respectively. At the beginning of these graphs the iSize bump height was set to a value far from an optimum one, and the feedback was intentionally turned off. At a time of $15^{\mathrm{h}}04^{\mathrm{m}}45^{\mathrm{s}}$ the feedback was turned on and the bump height started to increase. Within some 10 s, the HER vertical beam size was enlarged, while that of the LER shrank. Simultaneously, the ratio of the vertical beam-size of the LER to that of the HER approached the target value of 0.8. When the ratio reached the target value at $05^{\mathrm{m}}40^{\mathrm{s}}$, the luminosity recorded a maximum value. It took about 1 min from turning on the feedback. The response of the feedback depends on the machine tuning situation. The optimum target-value is obtained by a trial-and-error method, and is changed as a function of the LER beam current.

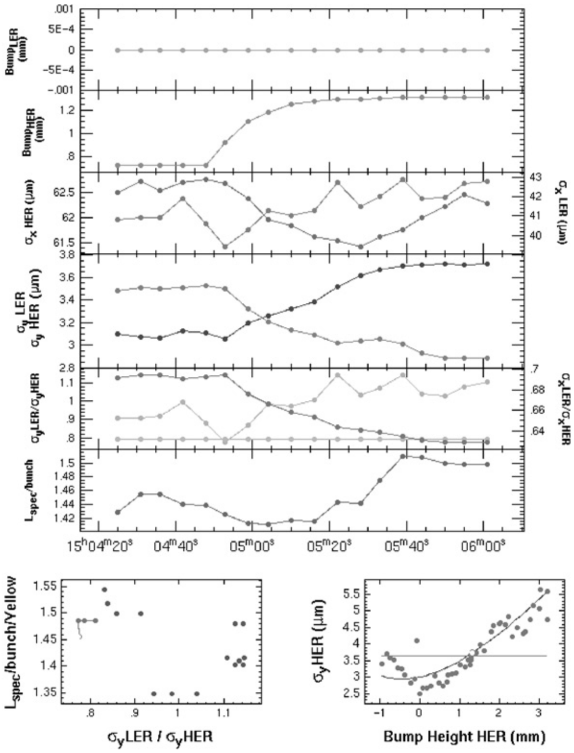

Fig. 27. The top two trend graphs correspond to the iSize bump heights for the LER (not used here) and HER. The middle two correspond to σ_x and σ_y. The red and blue lines express those of LER and HER for each direction. The fifth graph shows the vertical size ratio (green line) and the target value (yellow line). The bottom shows the luminosity measured by a CsI calorimetry in the Belle detector. The lower left and right of the figure show correlations of the luminosity with the ratio and σ_y^{HER} with the bump height, respectively.

5.4.4. Simulation

To understand the effect of the iSize feedback system, we performed beam–beam simulations for

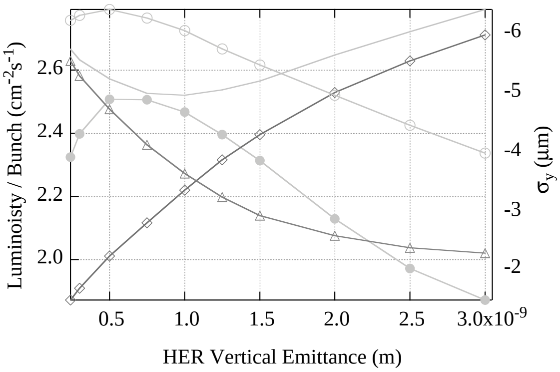

Fig. 28. Luminosity (yellow●), σ_y (red △(LER), blue ◇ (HER)) and Σ_y (green-) for a crossing angle of 22 mrad and luminosity (yellow ◦) for zero-crossing angle as a function of the HER vertical emittance.

Table 4
Parameters for the simulations

	LER	HER	Unit
Energy	3.5	8.0	GeV
ε_x	18	24	nm
$\varepsilon_y/\varepsilon_x$	2 (initial value) (1)	Controlled by iSize Feedback (1)	%
β_x^*/β_y^*	0.63/0.007	0.8/0.007	m
Bunch current	0.66 (0.87)	0.50 (0.37)	mA
Bunch length	5.5@6.0	5.7@11.0	mm@MV
ν_x/ν_y	45.518/44.063	44.525/42.135	

The values in ( ) are the designed values.

the present working parameters of KEKB with a code developed by Ohmi [13,19].

The simulation parameters are given in Table 4. Fig. 28 shows the luminosity and the vertical beam sizes of both rings as a function of the HER vertical emittance in the cases of crossing angles of 22 mrad (KEKB) and 0 mrad. The highest luminosity is obtained around the minimum value of Σ_y ($\equiv \sqrt{(\sigma_y^{\mathrm{HER}})^2 + (\sigma_y^{\mathrm{LER}})^2}$). And the HER vertical emittance dependence of the luminosity for KEKB is stronger than that for the case of zero-crossing.

We cannot directly compare the results of the simulation with the actual measurements for some reasons. One reason is that the simulations only deal with the beam–beam blowup, and we take no account of the single-beam blowup, which is actually observed in the LER. Another reason is that a calibration of the SRM is not yet completed. However, it is qualitatively shown by the simulations that there is an optimum value of the HER emittance as regards luminosity.

6. Beam background

The main purpose of the Belle detector is to make precision studies of B meson decays with a special emphasis on testing standard-model predictions concerning violations of *CP* symmetry [21]. The detector sits in the single interaction region (IR) of KEKB in the Tsukuba experimental hall.

Background from the beams is harmful for the detector system for three reasons;

- spurious signals from the background degrade the performance of reconstruction or resolution of measurements,
- background makes the transfer rate in a data-acquisition system higher,
- large accumulation of background radiation dose may result in a permanent damage of the detector components, such as read-out electronics, scintillation crystals and the sense wires in a wire chamber.

To keep the background below a tolerable level, we are recording information from PIN diodes and RADFETs (a real-time integrating dosimeter based on MOS technology [22]) located around the IP beryllium beam pipe, the pure CsI crystals placed at the entrance of the Belle detector to monitor the injection-related noise or the components of the Belle detector itself, as summarized in Table 5. We can investigate the nature of the background by careful comparisons among those informations in terms of their radial or azimuthal positions, energy response or timing characteristics.

The accumulated dose measured by the RADFET's in the period of 2000-Fall to 2001-Summer is plotted in Fig. 29. The front-end chip [23]

Table 5
Background monitors in Belle

Sensor/monitor	QTY.	Location	Function
PIN diode	8	IP beam pipe outer	Instant. dose meas., beam abort
RADFET	8	IP beam pipe outer	Accumulated dose meas.
PIN diode	8	SVD 1st layer LSI	Instant. dose meas., beam abort
RADFET	8	SVD 1st layer LSI	Accumulated dose meas.
Pure CsI crystal w/PMT	2	Beam entrance of Belle	Fast monitor for injection
CDC anode current	3	Inner/mid/outer layers	Monitor by gaseous detector
ToF counter rate	3	125 cm from beam	Monitor with plastic scint.
EFC counter rate	8	Tip of QCS cryostat	Monitor with BGO crystal

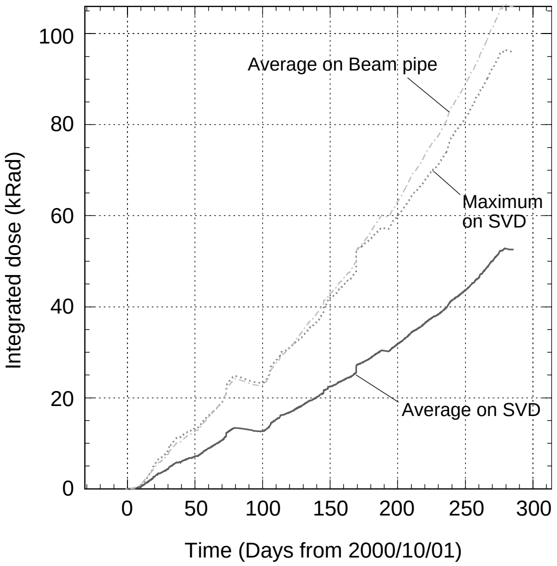

Fig. 29. Accumulated dose measured by RADFETS at the SVD location. The dotted-dash curve represents an average dose at the surface of beampipe. The dashed curve and the solid curve show the maximum and the average among the RADFETs at the SVD.

currently used in a silicon vertex detector (SVD) are radiation tolerant up to 1 Mrad, and the current rate of accumulation of the dose is not very uncomfortable.

6.1. Spent particle background

Most of the background at a practical beam current is thought to come from spent particles, which are losing their energy or changing their direction via interactions with residual gas molecules inside the beampipe of the ring. Some of those spent particles generated upstream of the IR hit the wall of the beampipe near the Belle detector and produce the background. Since the number of residual molecules is presumably proportional to the stored beam current, the background level should have a quadratic dependence on the current. Fig. 30 shows such dependences in either the LER or HER observed in a special background study with single-beam operation. This implies that the background due to synchrotron radiation from the magnets in the IR, which should be proportional to the beam current, is not dominant under the normal operation [24].

Several simulation studies for spent particles show that those generated anywhere in the ring could contribute to the background almost equally. It is also shown there that, once movable masks are installed in the arc section the predicted background can be dramatically reduced. The spent particles generated upstream of the mask would no longer have a significant contribution to the background.

A comparison of the contribution from the different section of the ring can be evaluated by a vacuum-pressure bump experiment, in which we intentionally make the vacuum pressure higher in a certain section of the ring and observe its effect on the background. The pressure-bump study made for the HER indicates that the relative contribution from the section opposite to the IR is very small, as shown in Fig. 31. In this figure, effective pressure-rises are evaluated indirectly from an inverse of the beam lifetime assuming

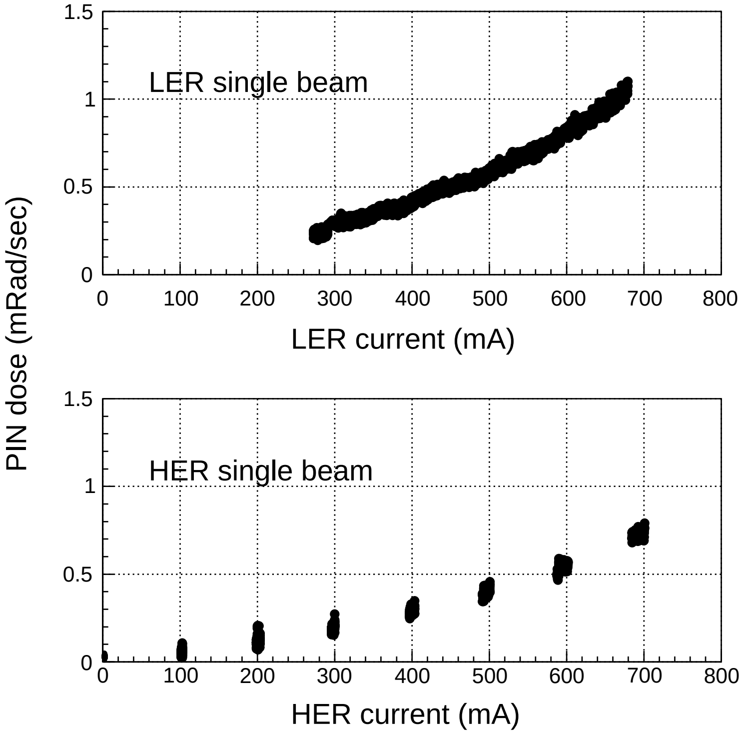

Fig. 30. Background for a single beam. The LER data was taken during a single storage period, while special discrete fills were made for the HER data.

that the lifetime is also determined predominantly by the interaction with the residual molecules.

In a similar experiment for the LER, we also observed that the contribution from the distant section is smaller than that from the section adjacent to the IR, although the difference is not as drastic as that observed in the HER. This may indicate that the background in the LER is not dominated by spent particles, as described in the next section. The relative contributions of several sections of the rings are tabulated in Table 6.

Table 6
Relative contribution of the vacuum pressure

Ring	Section	Relative contrib.
LER	Ring average	1
LER	Upstream of IR	3
LER	Opposite straight	0.5
HER	Ring average	1
HER	Upstream of IR	20
HER	Opposite straight	0.1

6.2. Other background source

During the beam collision operation, we often observe a sudden change in the background level without any change in the beam current or vacuum pressure. This suggests that there is background which is related not to spent particles generated by residual gas molecules, but to particles falling into the beam tail sensitive to the condition of the beam collision. It is very difficult to make a quantitative study of such a background, since the collision conditions are sometimes hard to reproduce.

In most of the cases, a clear decrease in the beam lifetime is observed when a jump in the background occurs. Fig. 32 shows such a dependence of

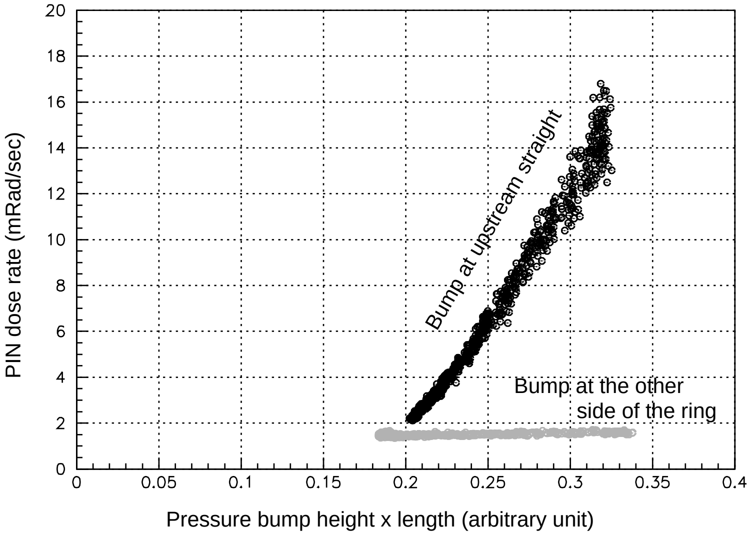

Fig. 31. Pressure bump at different places. The black dots represent the change in the background during a rise of the vacuum pressure at the upstream straight section. The gray dots show that for the bump at the opposite straight section.

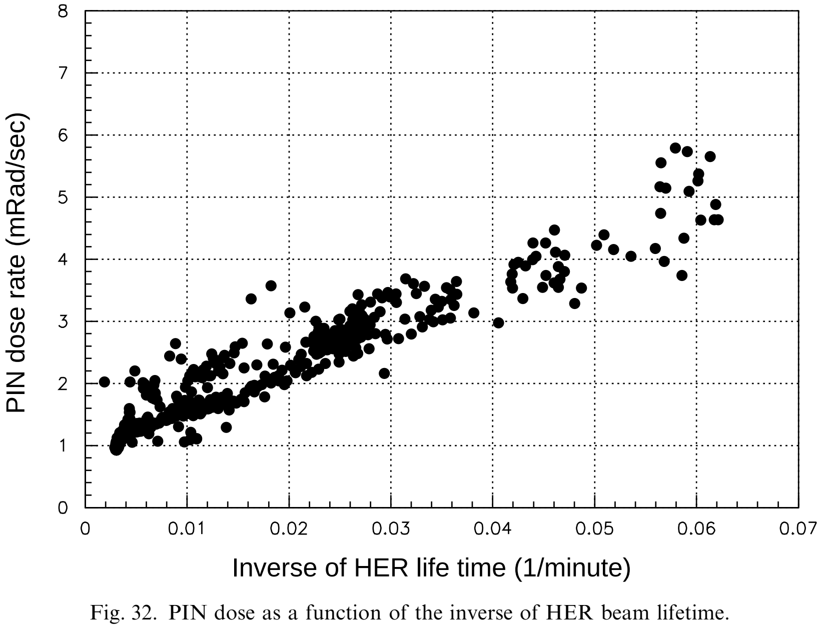

Fig. 32. PIN dose as a function of the inverse of HER beam lifetime.

the background measured in the PIN diode on the inverse of the HER beam lifetime during normal beam collisions. The lifetime reduction can be considered as *out-of-tune* state of the beam due to the beam–beam effect together with a limited acceptance somewhere in the ring. A clear correlation with the background in the figure indicates that the beam is lost near the IR.

We also observe a similar dependence of the background on the LER lifetime. It is found for

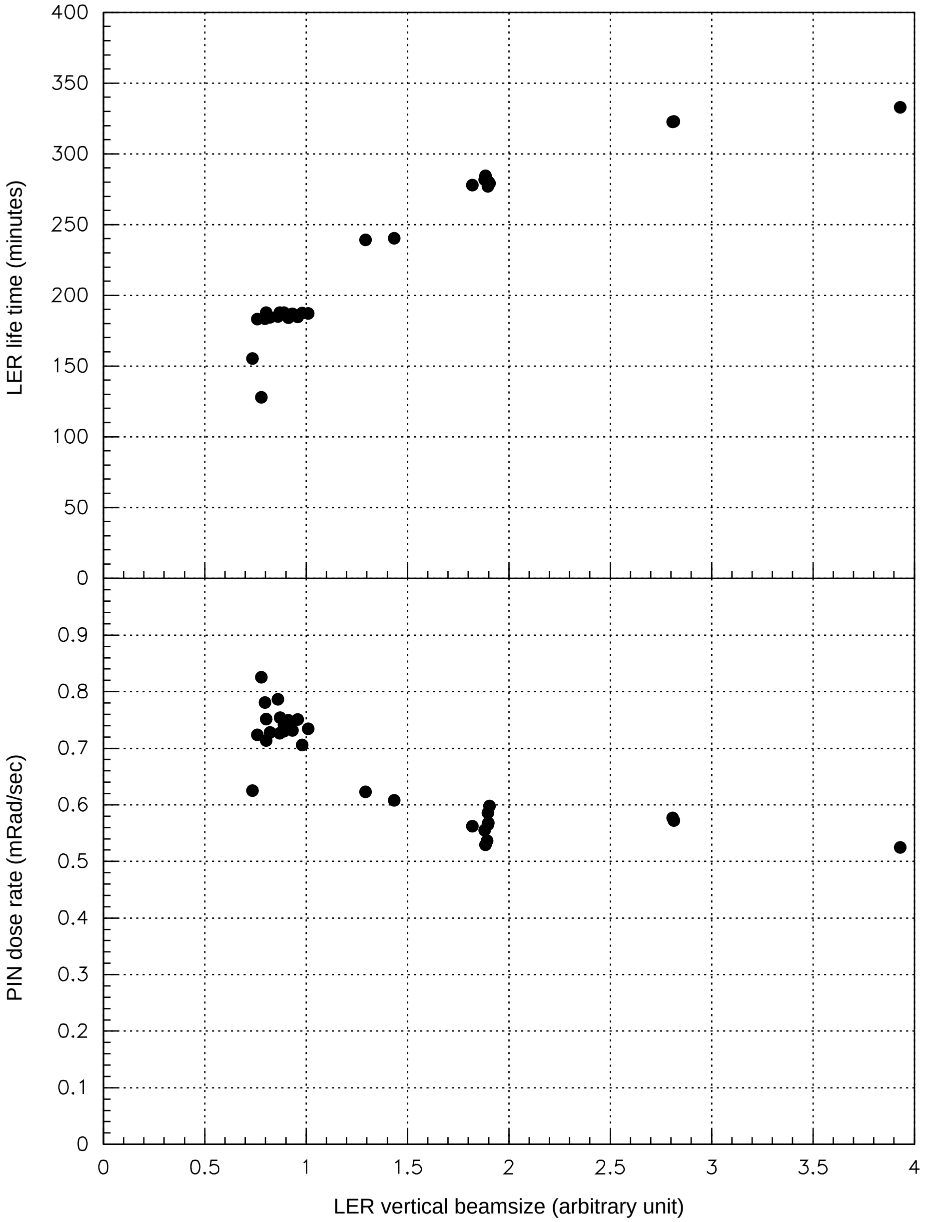

Fig. 33. Background and lifetime as functions of the LER vertical beam size. The beam size is varied by changing the vertical beam emittance.

the LER case that they are clearly correlated with the vertical beam size, as shown in Fig. 33. The relation between the beam lifetime and beam size (or particle density in a beam bunch) can be explained by the Touschek scattering. The figure suggests that some of the particles kicked off by the scattering are lost in the IR and produce the background.

With a significant improvement of the vacuum condition in both LER and HER, the backgrounds from the sources mentioned here are found to be very important.

7. Movable masks

A movable mask (or a collimator) is a device that cuts off particles escaped from a beam-bunch which can cause background in the physics-detector. As the name indicates, the head of the mask is movable (remotely controllable), so that we can carefully control a distance between the mask-head and the beam, while observing the detector-background as well as the beam lifetime. Sixteen movable masks were initially installed in the straight and arc section at the upstream-side of the interaction region.

As the stored currents increase, however, these masks began showing problems of heating and arcing due to the transient wall current or the intense RF fields of trapped modes [25]. The heating and arcing sometimes caused vacuum leaks. In addition, the trapped mode excited a strong longitudinal coupled-bunch instability and limited the stored beam current. The mask problems had been one of the most serious hardware problems in KEKB.

Since the problems were revealed, several types of masks were manufactured and installed to the rings, step by step. The history of these masks is presented in Fig. 34. The finally installed masks, Ver. 4 and 5, have been working almost as expected up to present. The generation of grooves on the mask head is, however, a still-remaining problem. To overcome the problem, an improved design of the masks will be tested in 2001. In this section we summarize the problems of the old masks (Ver. 1–3), and then report the present status of the latest ones (Ver. 4 and 5).

7.1. Problems of the old masks

A photo of an originally designed movable mask (Ver. 1) is shown in Fig. 35. The mask head is a block made of Cu–W and its inside is cooled by a water flow. The mask head attached to a stem is inserted from a side-port of the beam chamber to inside, and its position is adjustable. A stroke of this adjustment is about 20 mm and a vacuum bellows absorbs the movement. A spacer fills the space of a port and makes the chamber surface smooth. The stem, the spacer and the bellows are made of stainless-steel. Fixed and sliding shield fingers are at the gap between the spacer and the chamber, and between the stem and the spacer, respectively. The shield finger is made of a silver-coated Be–Cu. The shield finger should prevent the RF fields from intruding inside the structure. The basic structures of other old masks (Ver. 2 and 3) are the same as that of Ver. 1, but the mask head was made of pure copper.

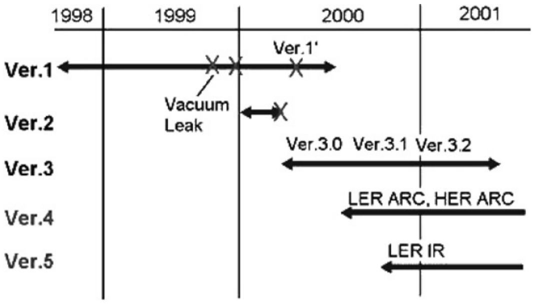

Fig. 34. History of the movable masks.

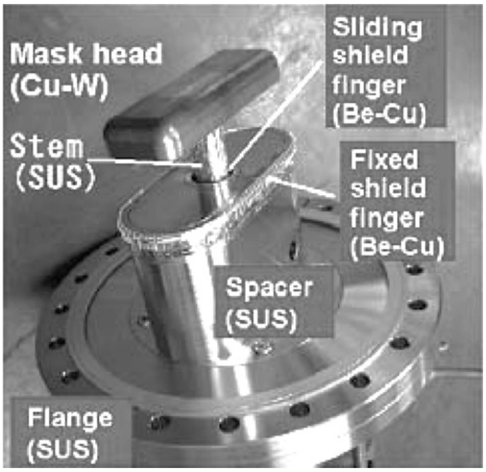

Fig. 35. Structure of the mask Ver. 1.

The first essential defect of the Ver. 1 was the sliding shield finger. It was too weak to withstand intense RF fields and was easily heated and melted. The insufficient cooling structure and the materials with low thermal conductivities worsened the heating problem. Once the sliding shield finger is broken, the RF field can easily enter the inside the spacer because of its coaxial-line structure. The extensive power of the entered RF field was dissipated at the bellows in a resonance condition. Furthermore, the broken fingers could be a seed of arcing between the spacer and the stem. We had experienced vacuum leaks four times with the Ver. 1 and 2 (see Fig. 34). Two cases were at the gap between the stem and the spacer, and another two cases were at the bellows. For the Ver. 3 series (3.0–3.2), the sliding shield fingers were moved toward the outside, as shown in Fig. 36, and the current density was reduced. The problems of fingers, that is, the excess heating and the vacuum leak, were solved after the Ver. 3.

The second serious defect of the Ver. 1, 2 and 3.0 was the lack of an effective absorber for the trapped modes of the mask. The *Q*-values of the major trapped mode of Ver. 1 and 2 are several thousand. Actually, we sometimes observed a longitudinal coupled-bunch instability when the mask head approached the beam. For the Ver. 3.1 and 3.2, therefore, SiC blocks were equipped as a higher-order mode (HOM) absorber, as shown in Fig. 36. The *Q*-values were reduced to less than 100. The problem of exciting beam oscillation was settled after the Ver. 3.1. However, operation for about 2 months at a beam current of over 700 mA resulted in a breakage of the SiC block. The power absorbed by the SiC block is estimated to be about 500 W, and a simulation suggests that the temperature was higher than 300°C at the highest, at a tip of the SiC block. There is a possibility that high thermal stress broke the block. The stored beam current in the HER, therefore, had been limited by the absorbed power at the SiC blocks.

The third problem, which is still a main problem of the latest masks (the Ver. 4 and 5), is grooves generated on the mask head, as shown in Fig. 37. The groove of the Ver. 3 is shown in this figure, but similar ones can be seen for the Ver. 4. The groove not only degrades the function of the mask, but also sometimes obstructs the injection beam by banks or whiskers around it (see Fig. 37). There was a danger of a water leak. A fast and safe beam-abort system was prepared using a PIN-diode loss-monitor, or by detecting a shift of the phase of the beam, though the improvement was not sufficient. This issue and the countermeasure are discussed in Section 7.2.3.

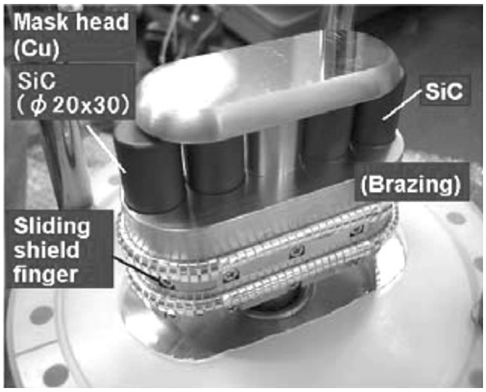

Fig. 36. Ver. 3.1 mask and the SiC HOM absorber.

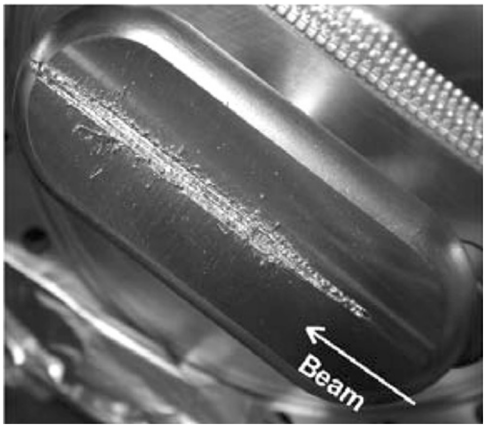

Fig. 37. Groove on the mask head.

7.2. New masks

7.2.1. Mask Ver. 4

The mask Ver. 4 was designed at first for the arc section of the LER. The structure is quite different from that of the old ones. A configuration of a set of vertical masks and the masks installed in the tunnel are shown in Figs. 38 and 39, respectively. The mask head is not a small block, as before, but

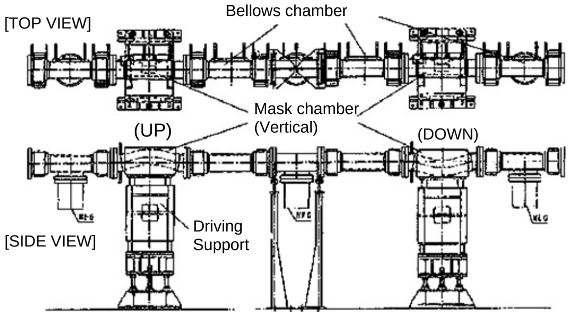

Fig. 38. Layout of Ver. 4 mask.

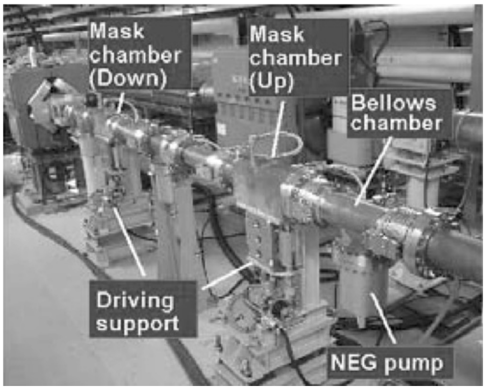

Fig. 39. A mask Ver. 4 installed in the tunnel.

a bent chamber (Mask chamber) with a driving support which moves the chamber; the chamber itself works as a mask. The chamber is made of pure copper. The movement of the mask chamber is absorbed by two universal bellows (Bellows chambers) connected at both sides of it. The most important feature of the Ver. 4 is that it has no trapped modes around the mask region, since the cross-section of the beam chamber does not change in this region. The Ver. 4 has shown no essential problem in the operation at beam currents over 800 mA, for about 1 year, since the Ver. 4 (vertical) for the LER, the horizontal masks (4 sets) for the LER and the vertical masks (8 sets) for HER were installed. By installing the HER vertical mask, a limit of the stored current was removed. The Ver. 4 horizontal masks for HER will also be installed in the near future.

However, the temperatures of the bellows located near the masks were found to be higher than those measured on the others bellows. The temperature depends on a bunch fill-pattern, a single-bunch current and the mask position (i.e. the shape of the bellows). Additionally, the heating showed a resonance-like behavior. The temperature rise, therefore, was considered to be due to a HOM (TE mode) excited at the mask chamber. The excited field can enter the space between the corrugation and the RF-shield finger of the bellows through narrow openings of the fingers, and dissipates the power. A simulation with MAFIA verified a heating mechanism. The bellows are now being cooled by small fans individually. The highest temperature at the designed full current (1.1 A) with the present bunch fill pattern is estimated to be about 90°C, and the heating may not be a serious problem.

7.2.2. Mask Ver. 5

The mask of Ver. 5 was developed and two of the masks were installed at the interaction region of the LER. Due to the spatial limitation, we could not use the Ver. 4 there. The structure (cross-section) of the Ver. 5 is shown in Fig. 40. The basic structure is a plunger used for the tuning of accelerating cavities. The mask head was made of pure copper. The mask damps the RF field heavily through its coaxial wave-guide structure loaded with a cylindrical SiC absorber (Fig. 41). The Q-factor of the Ver. 5 for the major trapped mode was calculated to be about 10, and the design power capability of the SiC absorber is up to 10 kW. Before installation, the mask received a high-power test with a 1296 MHz microwave, up to 4.2 kW. At a beam current of 500 mA, the

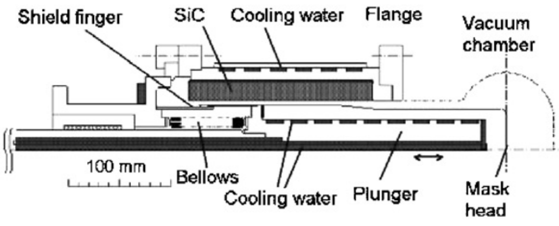

Fig. 40. Structure of the mask of the Ver. 5.

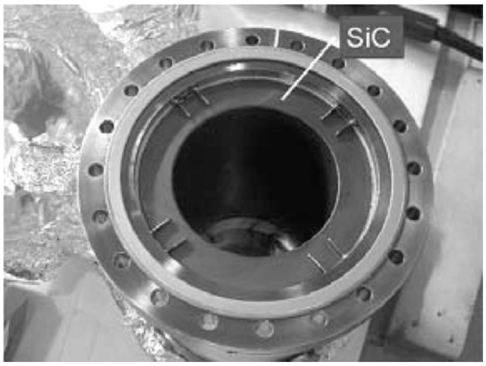

Fig. 41. Photo of the mask Ver. 5.

absorbed power is estimated as about 800 W, and thus the Ver. 5 should have no problem even at the design current, 2.6 A. The grooves on the mask head, however, should be checked regularly. Installation to the HER is now under consideration.

7.2.3. *Grooves on the mask head*

A remaining main problem is the grooves generated on the mask head (pure copper). The grooves seem to be made by an impact of the stored beam when the beam orbit was abnormally steered. It is also said that the energy loss of a beam particle due to a power-down of an accelerating cavity leads to a vertical beam oscillation or a beam-size blowup, and then causes digging of the mask head. Simulations were performed using the EGS4 program that can estimate the temperatures of several metals hit by a round electron beam. The result suggested that the temperature of copper exceeds the melting point after passing about one radiation length by the beam of several hundred mA, which is almost consistent with the observation (see Fig. 37). A light material, such as carbon, titanium or aluminum, can reduce the temperature-rise owing to its low deposit-energy density along the beam path. The energy-degradation efficiency of light materials, however, would also naturally decrease for a fixed geometrical length. Another simulation, on the other hand, suggested us that the material with a length of 1–2 in the radiation length is sufficient to satisfy the background-limit of the Belle detector for the masks at the arc section. Therefore, a trial mask head made of aluminum or titanium for the vertical Ver. 4 was designed (the Ver. 4.5). The total length corresponds to 1.1–2.4 radiation lengths. The whole structure is the same as that of Ver. 4. The mask will be installed in summer 2001 and tested in the autumn runs, in the HER.

8. Fabrication and installation of the solenoid coils in the LER

As we have described in Section 4, we installed a large number of solenoid coils to overcome the blowup problem observed in the LER. In order to carry out the design and installation of the solenoids, a task-force group was organized in June 2000. After extensive feasibility studies of two types, i.e., a permanent-magnet type and a solenoid-coil type, the latter was chosen. A design study of a solenoid coil which can produce about 50 G at an operation current of 5 A and its winding machine started at the end of July, 2000. A prototype coil and its winding machine were completed and a trial winding was successfully carried out at the end of August.

8.1. *Specification of solenoid coils*

We prepared two types of the solenoid coil: (1) a coil wound on a stainless-steel bobbin, which has an inner diameter of 15 cm and lengths of 10, 19, 25, 30, 40, 50, and 65 cm. This type of coils was installed in long free-space sections of the LER. (2) A short frame-less solenoid coil with an inner diameter of 22 cm for short free-space sections of the NEG pumps and the bellows. Fig. 42 shows the solenoid coil with a bobbin mounted on the LER vacuum pipe. Copper cable of 2 mm in diameter, which is electrically insulated by polyester varnish, is used for the coil winding. A double-layer coil is wound on a stainless-steel winding bobbin. The magnetic field on the center axis is 60 G with an excitation current of 5 A. The coil was installed on a beampipe using aluminum plates on the both ends of the coil. Fig. 43 shows the frame-less short coil mounted on the LER

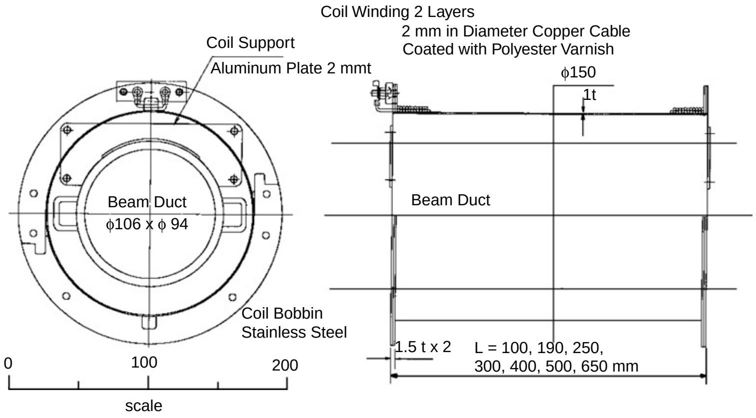

Fig. 42. Long solenoid coil wound on a stainless-steel bobbin.

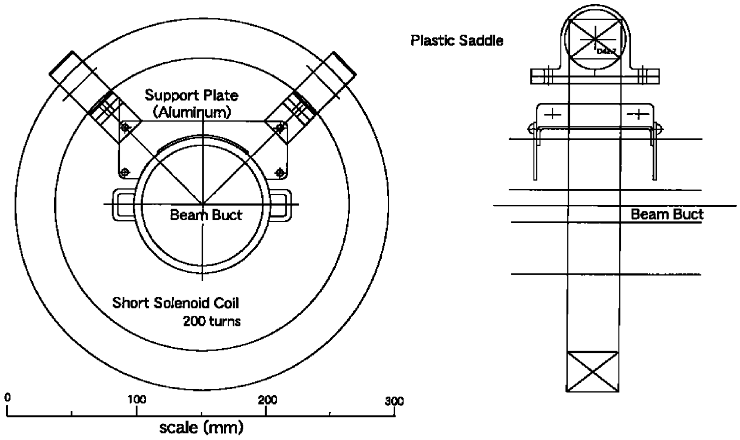

Fig. 43. Frameless short solenoid coil.

beampipe. This coil, having a total turn number of 200 with a 3 cm × 4 cm cross section was wound using the same copper wire as that used for the long solenoid coil.

8.2. Solenoid coil with a stainless-steel bobbin and its winding machines

A pair of parts punched from 1.5-mm thick stainless-steel (SUS304) is assembled into a half-end part of the bobbin by welding. A half-body of the bobbin is rolled from a 1-mm thick stainless-steel sheet. A full half-bobbin is assembled by welding. These two half-bobbins are assembled into a full bobbin around the existing beampipe with screws at both ends of the bobbin. Fig. 44 shows one kind of winding machine used for the long solenoid coil. The coil bobbin around the beampipe is connected to rollers of the winding machine, which is supported from the floor. A pair of rubber rollers, which are driven by a motor, turns the coil bobbin. Another type of winding machine, shown in Fig. 45, has also been developed. This winding machine can be attached directly to the beampipe. This facilitated the coil winding in a limited space.

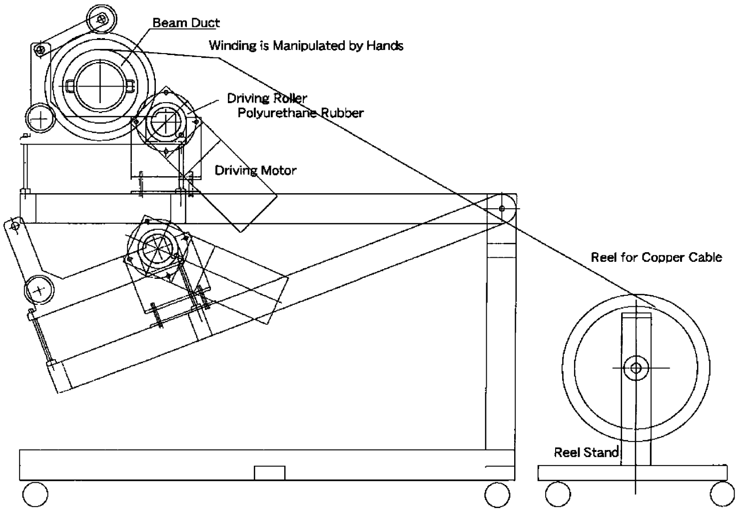

Fig. 44. Coil winding machine for a long solenoid.

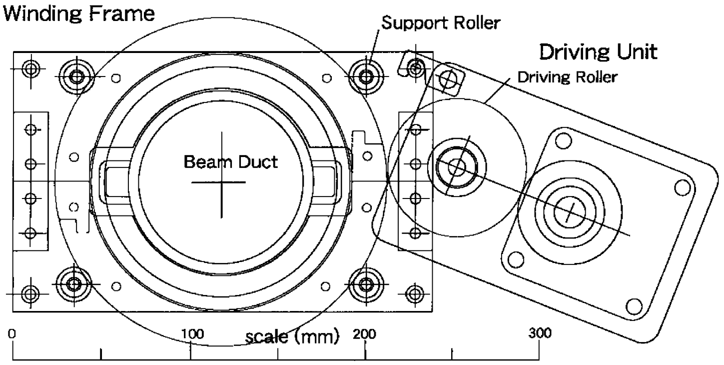

Fig. 45. Coil winding at congested part of the LER beampipe.

8.3. Frameless coil and its winding machines

At both ends of the NEG pumps and the bellows part, there are short free spaces, as shown in Fig. 46. In these accelerator sections only short-coil winding is available, because there is cooling water piping for the beampipe. Therefore, the frameless short solenoid coils with inner diameters of 22 cm were wound in these sections. Fig. 47 shows the winding machine used for the frameless short coil. The winding frame can be disassembled into four parts after the winding in order to remove the coil.

8.4. Coil winding

A total of more than 12 coil-winding machines for solenoid coils with bobbins have been fabricated to meet the requirements of winding a large number of coils in a short period of time. Assembly lines of the coil bobbins were constructed inside KEK to supply a large number of the bobbins, about 300 per day, in parallel with the coil winding. Modifications and improvements of the coil-winding machines, especially its support part, were carried out in parallel with the winding. The coil windings were carried out using about 10

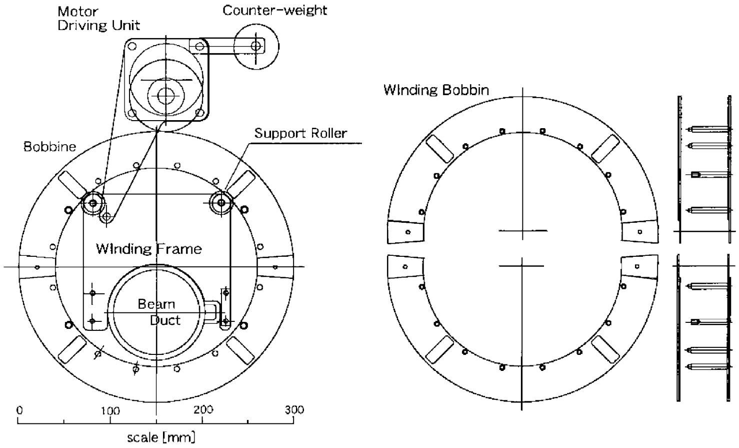

Fig. 46. Coil winding at congested part of the LER beampipe.

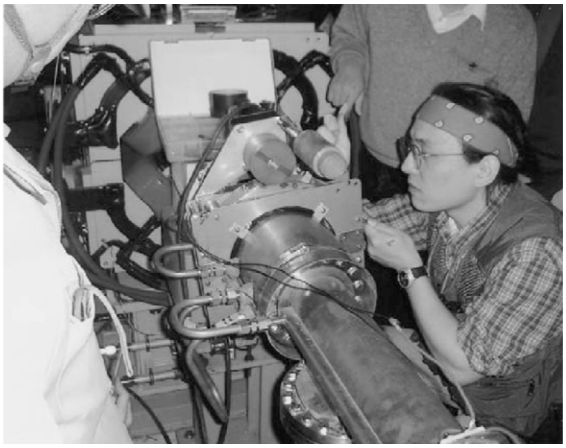

Fig. 47. Coil winding machine for a frameless short solenoid coil and its disassembled bobbin.

winding machines in parallel. A total of about 2200 solenoid coils was wound in the summer shutdown of 2000 in only 2 weeks. Another 550 coils were wound by hand on vacuum chambers of the steering magnets.

In some of the coils, electrical short circuits to the ground were found by a withstand voltage test of 500 V. These short circuits were caused by the punch rupture of the ground insulation film (25 μm meter thickness) by small metal fragments contaminated during assembling or a sharp edge of the connecting part of the bobbin. We have improved this weak point by removing the sharp edge of the bobbin and reinforcing the insulation of the connecting part. We rewound a total of about 100 coils. A total of about 1000 frameless short coils were wound by using 12 winding-machines in the winter of 2000–2001. A total of about 3300 coils, mostly frameless short coils but including about 30 long-solenoid coils with a bobbin, were wound in the summer of 2001.

9. Conclusion

KEKB has been recording a luminosity unprecedented in the history of colliders. It has faced a number of challenges related to various beam-dynamics and technical issues, most of which have been solved through the commissioning process. Remaining obstacles on the path towards the design luminosity, such as the electron cloud, will be studied more rigorously and—we expect—quickly overcome. This machine will continue increasing its luminosity to and beyond the design value, thereby extending the frontier of particle physics into hitherto unexplored territory.

Acknowledgements

The authors would like to give their thanks to Prof. F. Takasaki for his continuous encouragement throughout this work. They are grateful for the accelerator-operation clues from Mitsubishi Electric System & Service Engineering Co. Ltd. Finally, they would like to acknowledge the hardwork and efforts of the team who actually fabricated the solenoid bobbins.

References

[1] KEKB B-Factory Design Report, KEK-Report 95-7, 1995.

[2] K. Oide, H. Koiso, Phys. Rev. E 47 (1993) 2010;
H. Koiso, K. Oide, Proceedings of the Particle Accelerator Conference (PAC95), TAG11, 1995, p. 2780.

[3] http://www-acc-theory.kek.jp/SAD/sad.html.

[4] T. Mitsuhashi, et al., Optical diagnostics system for KEKB B-factory, Proceedings of EPAC2000, Vienna, Austria.

[5] K. Oide, et al., Proceedings of International Workshop on Performance Improvement of Electron–Positron Collider Particle Factories, KEK Proceedings 99-24, 2000, p. 12.

[6] H. Fukuma, et al., Observation of vertical beam blow-up in KEKB low energy ring, Proceedings of European Particle Accelerator Conference EPAC2000, Vienna, 2000, p. 1122.

[7] H. Fukuma, et al., Study of vertical beam blowup in KEKB low energy ring, Proceedings of High Energy Accelerator Conference HEAC2001, Tsukuba, 2001.

[8] F. Zimmermann, CERN-SL-Note-2000-004 AP, 2000.

[9] K. Ohmi, F. Zimmermann, Head–tail instability caused by electron cloud in positron storage rings, Phys. Rev. Lett. 85 (2000) 3821.

[10] Y. Ohnishi, et al., Study of fast ion instability at KEKB electron ring, Proceedings of European Particle Accelerator Conference EPAC2000, Vienna, 2000, p. 1167.

[11] E.A. Perevedentsev, A.A. Valishev, Phys. Rev. Special Topics 4 (2001) 024403.

[12] K. Ohmi, Private communication.

[13] K. Ohmi, et al., Phys. Rev. E 49 (1994) 751.

[14] Y. Wu, et al., HEACC 2001, Tsukuba, March 2001.

[15] M. Tejima, et al., Proceedings of e^+e^- factories '99, Tsukuba, Japan, 1999, p. 131.

[16] H. Fukuma, et al. Observation of vertical beam blow-up in KEKB low energy ring, Proceedings of EPAC 2000, Vienna, Austria.

[17] H. Koiso, K. Oide, in: Proceedings of the 16th IEEE PAC95, Dallas, TX, TAG11, 1995, p. 2780.

[18] T. Mitsuhashi, et al., Optical diagnostics system for KEKB B-factory, Proceedings of EPAC 2000, Vienna, Austria, 2000.

[19] M. Tawada, Y. Funakoshi, M. Masuzawa, H. Ohmi, Comparison of beam–beam simulation with experiments at the KEKB, EPAC 2000, Vienna, Austria, 2000, p. 1193.

[20] W.H. Press, et al., Numerical Recipes in C The Art of Scientific Computing, 2nd Edition, Cambridge University Press, Cambridge, January 1993, p. 564.

[21] K. Abe, et al., The Belle detector, KEK Progress Report 2000-4, Nucl. Instr. and Meth. A 479 (2002) 117.

[22] http://www.jratech.co.uk/tech_bank/techs/tcif161.htm.

[23] E. Nygrad, et al., Nucl. Instr. and Meth. A 301 (1991) 506; O. Toker, et al., Nucl. Instr. and Meth. A 340 (1994) 572.

[24] J. Haba, in: Proceedings of the International Workshop on Performance Improvement of Electron–Positron Collider Particle Factories (e^+e^- factories 99), Tsukuba, Japan, September 1999, p. 21.

[25] Y. Suetsugu, et al., Development of the movable mask system for KEKB, in: Proceedings of EPAC2000, Vienna, June 2000, p. 2301.